EUROPEAN ORGANIZATION FOR NUCLEAR RESEARCH

CERN-EP/79-51
30 May 1979

# A SPOT-FOCUSING ČERENKOV DETECTOR

M. Benot, J.C. Bertrand, A. Maurer and R. Meunier*)

CERN, Geneva, Switzerland

## ABSTRACT

Tests on a new type of Čerenkov counter have been carried out at CERN in a 50 GeV/c positive beam. This detector can be seen as a ring-focusing counter in which a subtraction of a fixed angle $\theta_0$ has been performed optically on the Čerenkov angle $\theta$. For a particular value $\gamma_0$ of the relativistic factor of the particle detected, the Čerenkov angle $\theta$ is equal to $\theta_0$, and all the Čerenkov light is focused on a spot, which gives its name to the detector. For all other values of $\gamma$ the spot degenerates into a small ring, much smaller than it would have been in a conventional focusing counter. The radius of the ring provides a determination of the velocity of the particle, and the position of the centre is related to its direction. This counter can be used for the detection of multi-particle events.

A description of the detector and its basic design principles are given. Results concerning the velocity resolution and light yield are also presented and compared with computed predictions.

(Submitted to Nuclear Instruments and Methods)

---

*) Visitor from the Centre d'Etudes nucléaires, Saclay, France.

## 1. INTRODUCTION

It has been shown in a previous paper [1] that it is possible to design a Čerenkov detector to provide simultaneously the direction and velocity of a charged particle coming from a small target or from a focused beam. Such a detector is based on an optical transformation of the Čerenkov light phase-space coordinates onto a two-dimensional light-sensitive array. This Čerenkov detector uses conical optics to focus the Čerenkov light from a particle with a Lorentz factor $\gamma_0$ into a small spot image. For a particle with $\gamma \neq \gamma_0$ a ring image is produced, the radius of which is related to the value of $\gamma$, and the position of the centre yields information on the angular coordinates of the particle.

For a given focal length of the system, the radius of the ring is much smaller than in the usual ring-focusing detectors but the resolution $\Delta\beta$ is of the same order, due in particular to the minimization of the optical aberrations and because of the compensation of the chromatic dispersion of the Čerenkov light. Such a detector is as fast as the ring focusing detectors.

For various reasons which are explained below, the prototype described here and which has been tested at the CERN Super Proton Synchrotron (SPS) is somewhat different from the one studied in ref. 1.

This prototype is of relatively short length, 3.8 m (to reduce its cost), and in order to keep the light yield to a reasonable level the nominal Čerenkov angle has been set to 35 mrad instead of 20 mrad, as quoted in the first studies [1].

For purely economical reasons the angular acceptance of this prototype has been limited to ±4.5 mrad but could easily be increased. The light is detected by an 11 × 11 matrix of 14 mm diameter R760 Hamamatsu phototubes. The equivalent focal length of the system is $\sim$ 20 m, making it optically equivalent (from the resolution point of view) to a DISC counter producing rings of about 1.4 m diameter.

This prototype has been tested in a 50 GeV/c positive beam, allowing the detection of $\pi$, K, p, and d. The tuning value $\gamma_0$ at which one could observe the spot-focusing effect could be chosen in the range $20 < \gamma < \infty$ by adjustment of the

pressure of the nitrogen used to fill the counter. The refractive index was monitored with a digital interferometer-refractometer immersed in the counter vessel itself.

## 2. GENERAL DESCRIPTION

According to the principles already described [1], a spherical mirror produces an image of the target position at a place where one must put a conical lens (axicon). In this case the spots or rings of Čerenkov light produced by this axicon are in the focal plane of the mirror and are virtual. All the performances simulated by computer in ref. 1 were analysed for this purely theoretical condition of virtual focus. It was assumed that in practice this virtual image would be focused as a real image in the plane of a light-detecting matrix by a suitable focusing system.

In the present prototype (fig. 1) the Čerenkov light hits the first main spherical mirror $M_1$ of 2 m focal length and is sent on to a second mirror $M_2$ (spherical to first order) after a 90 degree deflection by a plane mirror $M_p$ and refraction in the axiconic lens. After further reflection the light crosses the axicon a second time, passes through a hole in $M_p$, and is focused on a fused-silica optical window W of 55 mm diameter. This part of the optics defines a "first stage" producing a primary real image (referred to in the rest of this paper as the "primary image") and has an equivalent focal length of 1 m. The exact position of this primary image plane can be adjusted to coincide with the plane of the photocathode of a multianode phototube or image intensifier of about 40 mm useful diameter. In fact, the multichannel multianode phototube available to us was not sufficiently reliable and we had to use an alternative technique [2]. We have instead used a matrix of phototubes as mentioned above, which, when provision is made for their individual mu-metal shielding, can be arranged on a 16 mm pitch matrix. This phototube matrix is too large and its pixel (picture element) size too coarse to install it at the first focus. We therefore had to project this primary image onto a matrix of square field lenses by means of a special-purpose transfer lens TL. Finally, the light is detected by the matrix of phototubes, the position of which is such that the exit pupil of the transfer lens is

focused by each field lens on the photocathode of the corresponding phototube. The image produced by the transfer lens is called here the "secondary image". It should be noted that the system used, namely an axicon and focusing mirror, is optically equivalent to an axicon of twice the bending angle, followed by a focusing optics equivalent to the mirror $M_2$.

The detector described in the previous paper [1] was restricted to a spherical mirror $M_1$ and an axicon doublet only. The image produced by such a configuration is virtual and is situated in the focal plane of $M_1$. Here the role of $M_2$ is to produce a primary real image, and the transfer lens TL allows us to accommodate large-size detectors like our matrix of photomultipliers.

The mechanical design of the field lenses and phototube support and the optical characteristics of the transfer lens are such that the global equivalent focal length of the counter can be adjusted to 10, 20, 30 or 40 m.

Increasing the equivalent focal length of the counter would improve the velocity resolution $\Delta\beta$ of the detector, but would reduce the angular acceptance of the counter by increasing the angular range beyond which the Čerenkov light falls outside the matrix. At the primary focus, on the optical window W where the equivalent focal length of the system is 1 m, the angular acceptance is ±20 mrad. The particles emitted in this cone cross the counter window and the main spherical mirror, the thickness of which is reduced to 10 mm in the central zone crossed by these particles. The counter windows are made of mylar sheets (or 2 mm Al when high pressure is needed). The counter is designed to work with nitrogen, helium, or a mixture of the two at pressures of up to 15 atm.

## 3. THE AXICONIC OBJECTIVE

### 3.1 Basic design principle

The axicon is the main optical element which characterizes a spot-focusing detector (SFD) and distinguishes it from a conventional-focusing Čerenkov counter.

An axicon with a straight meridian, i.e. limited by a conical surface, is not the only possible shape for the corrector. This optical element can be generated by an arc of a circle, in which case it can be more exactly referred to as a toroid.

In the thin-lens approximation a toroid is equivalent to the combination of an axicon and a spherical lens, which may also be an interesting solution, since a focusing element must be combined with the axicon to produce real images at the primary focus. For this counter we have chosen to use an axicon doublet and an aspherical mirror to focus a real image on the optical window of the detector.

It has been shown in ref. 1 that an axicon doublet is needed to fulfil simultaneously the conditions of spot focusing and of correction of the chromatic dispersion of the Čerenkov light. A cemented doublet is preferable not only because it improves the light transmission but also because it places less stringent requirements on the surface accuracy at the interface. In fact, it can be seen that an error $\Delta\alpha$ of the axicon angle $\alpha$, in a given region of the surface crossed by a meridian ray, introduces an error $\delta d$ in the deviation such that

$$\frac{\delta d}{\delta \alpha} \sim \Delta n_{12} \ ,$$

where $\Delta n_{12}$ is the difference between the indices on each side of the interface. When one of the media is a gas, this quantity is three to four times larger than at an optically cemented surface.

In general, making such a doublet implies the grinding and polishing of at least three conical surfaces, as the fourth one can always be a plane one. However, the making of such surfaces is a rather delicate and expensive task and it is therefore useful to see whether the two axicons could both have a plane face, which means, for a cemented doublet, that their apex angle is of equal magnitude and opposite sign.

For the required design the basic relations are [1]

$$(\bar{n}_g - 1) \sim \frac{\theta_0^2}{2} + (1 - \beta_0) \sim \frac{\theta_0^2}{2}\left(1 + \frac{1}{\gamma_0^2\theta_0^2}\right) , \qquad (1)$$

where

$\bar{n}_g$ is the refractive index of the gas, for the average wavelength of the useful spectrum $\bar{\lambda}$;

$\theta_0$ is the Čerenkov angle at this wavelength;

$\gamma_0$ is the nominal $\gamma$ value for which one wants spot focusing.

The chromatic dispersion is

$$\Delta\theta_0 \sim \frac{\theta_0}{2\nu_g}\left(1 + \frac{1}{\gamma_0^2\theta_0^2}\right), \tag{2}$$

where $\nu_g$ is the Abbe number of the gas:

$$\nu_g = \frac{\bar{n}_g - 1}{n_g(\lambda_1) - n_g(\lambda_2)} ; \tag{3}$$

$\lambda_1$ and $\lambda_2$ are the two achromatization wavelengths of the useful spectrum, and $n_g(\lambda_1)$, $n_g(\lambda_2)$ the corresponding values of the gas index of refraction. Our optical design follows the classical concept of achromatism for two selected wavelengths because of its simplicity and usefulness, but we should not overlook the necessity of a careful secondary spectrum optimization. The angular deviation $d(\lambda)$ of a light ray by a symmetric axicon doublet of refractive indices $n_1$ and $n_2$ is given by

$$d(\lambda) \sim \alpha\{[n_1(\lambda) - 1] - [n_2(\lambda) - 1]\} . \tag{4}$$

In the present case, where the target is positioned at the centre of curvature of the first mirror [1], the condition for spot focusing is

$$d(\lambda) = \theta_0(\lambda) . \tag{5}$$

Moreover, since the chromatic dispersion must be cancelled, this can be written

$$d(\lambda_1) - d(\lambda_2) = \Delta\theta_0 . \tag{6}$$

Combining eqs. (1) to (6), it is found that

$$\theta_0^2 = \mu\, \Delta n_g , \tag{7}$$

with

$$\mu = \frac{\bar{n}_1 - \bar{n}_2}{\Delta n_1 - \Delta n_2} , \tag{8}$$

where

$$\Delta n_i = n_i(\lambda_1) - n_i(\lambda_2) ,$$

$$\bar{n}_i = n_i(\bar{\lambda})$$

Then

$$\alpha \sim \frac{\theta_0}{\bar{n}_1 - \bar{n}_2} . \tag{9}$$

Equation (7) can be rewritten

$$\theta_0^2 \sim \mu \frac{n_g - 1}{\nu_g} . \tag{10}$$

In our case from formulae (1) and (10) we have

$$\nu_g = \frac{\mu}{2}\left(1 + \frac{1}{\gamma_0^2\theta_0^2}\right) . \tag{11}$$

It follows that once $\theta_0$ and $\alpha$ have been fixed, if it is necessary to tune the counter in order to have spot focusing for various possible values of $\gamma_0$, it must be done by proper setting of $(n_g - 1)$ according to (1), but also the $\nu_g$ of the gas must be adjusted each time in order to satisfy (10). This can be done by varying the gas composition and its pressure.

In practice there is a limited choice of materials which can be used for the axiconic lens, as they have to be sufficiently transparent in the useful wavelength range considered, i.e. about 250 nm to 500 nm, where we have chosen the following design values:

$$\text{achromatization wavelength} \begin{cases} \lambda_1 = 440 \text{ nm} \\ \lambda_2 = 250 \text{ nm} \end{cases}$$

$$\text{mean wavelength } \bar{\lambda} = 350 \text{ nm} .$$

Fused silica is the most convenient medium because it is not birefringent, it is

available in pieces of sufficient size and at a reasonable price, and it can be ground and polished almost as easily as glass. Monocrystals of NaCl are also adequate and have in fact been used in the construction of high-performance DISC counters [3,4] where the chromatic dispersion correction is made adjustable according to the $\gamma$ of the selected particles. However, the peculiarities of the present design have led us to consider the use of water and fused silica. Water is indeed a rather good and convenient medium which has been used here for the design of both the axiconic objective and the transfer lens.

The $\mu$ value for the doublet $H_2O$-$SiO_2$ is

$$\mu = 36.597 \ , \tag{13}$$

and the nominal value chosen for $\theta_0$ (see section 1) is

$$\theta_0 = 35 \text{ mrad} \ . \tag{14}$$

In fact, as seen in fig. 1, the light crosses the axicon doublet twice. It is thus designed for a deviation of $\theta_0/2$. This solution, based on the use of a second mirror $M_2$ to produce on the optical window a real image of the desired size, offers the important advantage of implying a shallower shape and therefore a thinner lens.

The apex angle $\alpha$ of the fused-silica axicon has been set to 137.0 mrad, which is very close to the first-order value obtained from formula (9). The exact value of this angle is not important, as the ray-tracing program provides the exact value of $\theta_0$ for which the detector is tuned.

The outer diameter of the objective is 300 mm, and this is still a reasonable size.

The mirror $M_2$ has a focal length of 1.333 m, and the design has been optimized by ray-tracing (see section 3.2) to include in particular a plane-parallel $SiO_2$ plate, the inner face of which is used as the plane interface with the axicon water lens.

The chromatic dispersion of a mixture of gases [such as $CH_4$, $\nu = 15.4$; air, $\nu = 20.66$ (or $N_2$); $SF_6$, $\nu = 35.53$; He, $\nu = 54.52$] in fact matches the chromatic correction of the objective quite well over quite a large range of $\gamma$ values. Table 1 shows the values of $(n_g - 1)$ for spot focusing and of $\nu_g$ as a function of $\gamma_0$ for $SiO_2$-$H_2O$ and with $\theta_0 = 35$ mrad.

It can be seen by interpolation that air, at atmospheric pressure, allows a tuning value $\gamma_0$ of 79.6, with $(n_g - 1) = 281.35 \times 10^{-6}$ and $\nu_g = 20.66$.

It is interesting to look at the amount of residual primary chromatic dispersion introduced when working with $N_2$ at various pressures in order to achieve the spot-focusing condition for different values of $\gamma_0$. If the counter is correctly compensated for $\gamma_0 = 80$, for example, the residual primary dispersion for $\gamma_0$ is given by

$$\delta_{chr} = \frac{1}{2\nu_g\theta_0}\left(\frac{1}{\gamma_0^2} - \frac{1}{\gamma^2}\right) . \tag{15}$$

In the present case this relation becomes

$$\delta_{chr} = \left(\frac{692.25}{\gamma^2} - 0.108\right) \text{ mrad} . \tag{16}$$

This residual chromatic error is not negligible; the gas composition must be adjusted to $\gamma_0$, although this is not very critical. For the present test we have used only $N_2$.

The extremely small variation of the ratio of the refractive indices of $SiO_2$ and $H_2O$ in our range of interest (from 1.09398 to 1.09512) explains the achromatic properties of this doublet. In fact the secondary spectrum is, in the present case, about five times smaller than what it would be with a $SiO_2$-NaCl combination. It is only when the bending angle is about comparable to the Čerenkov angle that the chromatic dispersion of the Čerenkov light can be corrected by such a combination. This is not the case, for example, in a DISC [3,4] where the corrector is a zero deviation element and requires a strongly dispersive combination such as $SiO_2$-NaCl, although the secondary spectrum and the inconvenience of using NaCl make this

combination less favourable. In the present case, the losses due to reflection at the interface, as given by the Fresnel relation, are particularly small:

$$R = \left( \frac{\bar{n}_1 - \bar{n}_2}{\bar{n}_1 + \bar{n}_2} \right)^2 = 2.5 \times 10^{-3}. \qquad (17)$$

3.2 Optimization of the design

The design of the axiconic objective has been optimized by direct ray-tracing using a simulation program which generates Čerenkov light along the particle trajectories with the three wavelengths defined in eq. (12).

The optimization for a particle is done along the optical axis; $N_2$ and He having been chosen for the mixture, the angle $\alpha$ is also given, as well as the $\gamma_0$ value. The program then works out the Čerenkov angle $\theta_0$ and the exact proportion of gas needed to produce the desired conditions of spot-focusing and chromatic angular dispersion compensation.

The exact position of the axicon and of its associated mirror, and the geometric aberrations, are optimized by studying the size of the spot produced in the primary image plane. The position of this plane is found by the program. The spherical aberration has been minimized by slightly "aspherizing" the mirror of the axiconic objective. The assumed shape of the mirror is defined by a meridian of the type

$$X = \frac{H^2}{2R} + \frac{1+\varepsilon}{8R^3} H^4 + \frac{1+\varepsilon'}{16R^5} H^6 , \qquad (18)$$

where H is measured perpendicularly to the optical axis and R is the radius of curvature at the apex of the surface. (A perfect sphere in the neighbourhood of the apex would be represented in the above development by making $\varepsilon = \varepsilon' = 0$.) The optimization process consists, then, in finding the values of $\varepsilon$ and $\varepsilon'$ for which the spherical aberration is minimized. This gives a raised-edge-shaped mirror, and the maximum departure from a sphere is 8.5 wavelengths at points a 100 mm from the optical axis. Table 2 gives the optical specifications of the SFD.

We have demonstrated [1] and, indeed, observed by simulation, that for particles which are not emitted from the centre of the target, i.e. with a non-negligible impact parameter, the light rays in the image lie on fourth-order curves. The departure of these curves from a spot, or a circle, is larger as the rays are emitted nearer to the target. These rays cross the axicon near the apex. It is therefore necessary, in order to reduce such aberrations, to create a dead region ahead of the target where no useful light can be emitted. In practice, in our tests, we have introduced a gap between the focus of the beam of particles and the counter body itself. In any case, when the counter is used in an experiment a space is required between the target and the counter for the installation of apparatus such as magnets, a vertex detector, scintillation counters, wire chambers, etc. Such a dead space is optically matched with the central hole in the axicon defining the forbidden region for the light.

In the present case this corresponds to a reduction of the radiator length, and therefore of the light produced, of $\sim$ 20%. The length of this region has been fixed by ray-tracing simulation.

It is also by means of this simulation that the size of the central hole in the plane mirror $M_p$ (fig. 1) has been determined. This central hole is particularly critical as it acts twice as a diaphragm on the light path. There must be a good match between the angular acceptance of the counter as defined by the first mirror, by the hole in the plane mirror, and by the axiconic objective. Indeed, vignetting due to the plane mirror starts for particles with a divergence > 15 mrad, and the vignetting amounts to $\sim$ 20% at 20 mrad.

However, owing to the limited size of the photodetection matrix (see section 4) chosen for the tests presented here, the actual acceptance of the counter, which is ±4.5 mrad, is not affected by this problem.

Because of the relatively small number of optical components used in this objective and because of the various constraints we have introduced, it is not possible to further reduce the remaining aberrations in the primary image. The

main aberration here is coma, which could have been reduced by changing the angle which the surfaces of the axicon doublet faces make with the axis; and this is precisely what we did not want to do, in order to have plane external faces.

## 4. THE TRANSFER LENS

### 4.1 General characteristics of the transfer lens

The Čerenkov light flux finally transmitted to the photomultipliers is proportional to the radiator length. It is then particularly important to transmit as much as possible of the produced light to the phototubes in order to keep the counter length to a minimum compatible with an acceptable photoelectron yield.

The transfer lens must therefore be free of vignetting, it must have the required numerical aperture, and have a good transparency in the range considered here [see eq. (12)].

A field lens in optical contact with the optical window W (fig. 1) is used to image, without light losses, the axicon objective on the entrance pupil of the transfer lens. For practical reasons the focal distance has been fixed to be about 100 mm, and the numerical aperture needed, depending slightly on the exact equivalent focal length of the lens, was 3.5. The achromatic correction had to lie in the same range as for the first stage of the optics (see section 3.1), i.e. in the near UV.

Such a lens is not readily available commercially and had to be specially designed by us.

As in the future we do not expect to enlarge the detector matrix to more than 500 to 1000 pixels, the field in the object space does not need to be larger than 30 mm diameter. This relatively modest field size was of considerable help for the design.

The media chosen for this design were $SiO_2$ and $H_2O$, as for the axiconic objective. Such a combination has good optical transmission characteristics over the wavelength range of interest, and it reduces the number of lenses which have

to be made. Moreover, if one manages, as is the case here, to have no air gaps between lenses, it makes antireflection coating unnecessary except on the two external faces, with, however, an extremely favourable Fresnel factor at the interfaces [see eq. (17)].

The main drawbacks of such a combination are: the small refractive index differences leading to large geometric aberrations; and the large temperature coefficient of the refractive index of water, but the temperature variations in the experimental hall were acceptable for our application.

4.2 Transfer lens design

We started the design with a basic system chromatically corrected and aplanatic for a combination point-infinity, thanks to an aspheric surface (Descartes oval) and an aplanatic spherical interface $SiO_2$-air on the short conjugate side. The other $SiO_2$-air interface was plane. Such a basic system could be symmetrized in order to make it a relay lens with twice the original power.

Such a starting design cannot entirely satisfy the conditions of achromatism and aplanatism, as these two conditions demand slightly different radii for the $SiO_2$-air interfaces. Since we did not want to use aspheric surfaces, we tried to replace them by strongly curved spherical surfaces [5], which finally became thin menisci having a common centre of curvature. Reduction of the spherical aberration was possible only by splitting the central lenses. The optimization process was based on a ray-tracing program using 20 rays and 3 wavelengths. One of the difficulties encountered was the impossibility of using a diaphragm to reduce some aberrations, because of the undesirable vignetting effect which it could introduce.

When an acceptable solution had been found, we evaluated the effect of small variations of thickness and curvature of each element on the various optical aberrations. The choice of the final values was determined by requiring that all rays fall inside a circular region corresponding to the spot size produced at the primary focus by the first-stage optics (table 3). The discrete and coarse

character of our detection matrix, and the need for the highest possible resolution for the counter, dictates this condition. It is preferable to have a sharply defined spot, even if it is large, than a bright spot accompanied by flares.

As could be expected, the final design of the transfer lens shows appreciable residual errors. The low refractive indices and their small differences lead to very strong curvatures, and high-order aberrations sharply limit the maximum aperture of the lens. In fact we have extended it slightly more than would have been the case in a conventional lens in order to accept all the Čerenkov light. This is clearly visible in fig. 2 when one compares the spot size for different F numbers. Most of the spot size is accounted for by the lateral colour, which could be attenuated only by reducing the total thickness of the transfer lens; but the correction of the astigmatism which dominates the field curvature [although this system presents a favourable Petzval radius of curvature (R = 2.89 × equivalent focal length)] requires the use of components with relatively large separations along the optical axis. Therefore a compromise had to be reached which partially satisfies these contradictory requirements.

### 4.3 Performances and construction of the transfer lens

This lens accepts nearly the full aperture up to the maximum necessary field angle of $\sim$ 150 mrad; it is also a nearly symmetrical system optimized for infinite conjugate (figs. 2 and 3). Figure 2 shows that the spot size of the transfer lens is a good match to the first-stage optics up to a field angle of 150 mrad corresponding to a particle divergence $\tau \approx 15$ mrad.

The various components were mounted in a stainless-steel barrel passivated with hot nitric acid and then filled with bidistilled water under vacuum. Only the external faces were antireflection coated for 350 nm with a $\lambda/4$ layer of $MgF_2$. Tests of this lens on the optical bench have shown good agreement between the computed performances and the measurements. Its equivalent focal length is 94.24 mm and the numerical aperture is F/3.45. It has been set up with a magnification of ×20 for this test run. Although, as shown in fig. 3, this lens is composed of

16 surfaces, the measured transmission indicated in table 4 is better above 405 nm than the transmission of a single uncoated $SiO_2$ lens.

### 4.4 Transfer lens for future SFD

These studies can be used as a starting point for the design of an axicon + focusing lens which would replace the double-pass axicon + aspheric mirror of the present design. In this case the equivalent focal length of the optics is large enough to accommodate directly a phototube matrix placed at the primary focus, with a considerable improvement in the light transmission. The F number of this focusing lens, of about F/6, will allow much better optical corrections.

## 5. CONSTRUCTION AND ADJUSTMENT OF OPTICAL ELEMENTS

The slightly aspheric mirror $M_2$ (fig. 1) made of Zerodur*), chosen for its ease of shaping and testing, was first polished spherical and then figured in the required region between the centre and the outer edge. Tests were done by interferometric measurements of the gap between the mirror profile and a spherical convex test plate, which had been designed to touch at the centre and the outer edge of the mirror simultaneously. The fringe pattern produced was compared to a template on which was shown the expected radial distribution of eight fringes corresponding to the desired profile of the mirror.

The $SiO_2$ axicon and the flat window needed to make the $H_2O$ axicon (fig. 2) are made of Spectrosil B**). The conical face was first generated at CERN on a milling machine using a bell-shaped diamond grinding tool 80 mm in diameter. At this stage irregularities along a generator were found to be less than 1 μm.

Difficulties occurred during the polishing stage, and some astigmatism was observed making necessary a second grinding operation before final polishing***). During polishing, tests were made by observation of the fringe pattern produced between the conical surface and a reference glass cylinder.

---

*) Manufactured by Jenaer Glaswerk Schott & Gen., Mainz, Germany.

**) Manufactured by Thermal Syndicate, Ltd., Wallsend, Northumberland, England.

***) All the precision optical surfaces have been polished at Optical Surfaces, Ltd., Kenley, Surrey, England.

After polishing it was found that radial and circumferential errors on the cone were less than $\lambda/2$ except for a turned-down outer edge (on a $\sim$ 2-3 mm wide annular zone) and a circumferential error of $\sim \lambda$ close to the inner edge.

Laboratory tests were performed with the complete axiconic objective mounted on a bench, by observation of the circle produced by a point source, using the objective in the reverse optical path mode.

The point source was produced with a laser and a microscope objective. With this method inhomogeneities were found in an annular zone, about 3 cm wide, near the outer edge of the axicon. Local reflection errors have been measured using a perforated screen. Local errors of irregular aspect, amounting to an error of $\sim$ 0.1 mrad on the deflection, have been observed over areas the total of which is less than 10% of the total useful area of the lens. They are distributed in the inhomogeneous annular zone mentioned above, and there may be a relation between these two defects.

The external faces of the axicon doublet have been antireflection-coated under vacuum below $10^{-7}$ Torr with a $\lambda/4$ layer of $MgF_2$, matched to a wavelength of 350 nm. The reflecting surfaces have been flash-coated with a 500 Å thick aluminium coating and coated immediately afterwards with a $\lambda/2$ $MgF_2$ layer, and then soaked in pure $O_2$ for 5 min.

These elements are mounted in steel barrels. The mirrors $M_1$ and $M_2$ (fig. 1) are each held against three lead inserts, and they are spring loaded at the back. They are also centred in their barrel by teflon stubs pressed against the mirror side.

Tests on mirror $M_1$ using the knife-edge method have shown that, when mounted in its barrel, there are no appreciable distortions as these are well within the $\lambda/8$ tolerance.

The plane mirror $M_p$ cut in an available stock of 12 mm thick glass shows some evidence of sagging under its own weight. This was certainly the reason for the slight astigmatism found in the well-focused image of a spot during our tests.

The different optical elements have been aligned and centred in the counter with the help of a He-Ne laser, and the secondary focus was adjusted by auto-collimation. To this end a 130 mm diameter plane mirror was inserted at the focal plane of mirror $M_1$ and carefully aligned perpendicularly to the axis on which the centre of curvature of $M_1$ had already been adjusted. The focusing at the first focus was performed with the red laser light, and also with the green light of a light-emitting diode (LED).

It is an easy matter to align the counter in the experimental hall in a beam line. Only the target position, i.e. the centre of curvature of the main mirror, needs to be put on this line. This is achieved by removing the front thin pressure window and by finding the position of a pin-point object which is imaged on itself by $M_1$.

## 6. THE PHOTODETECTORS

The number of detected photoelectrons, when the detector is set for spot focusing, is given by

$$N = AL\theta_0^2 \ , \tag{19}$$

which in our case, where the radiator length L is 360 cm and $\theta_0$ = 35 mrad, becomes

$$N = 0.441 \times A \ ,$$

where A is a figure of merit which characterizes the photodetector efficiency and the light transmission efficiency of the optics.

The present design was based on the intention to use a multianode photo-multiplier (MPM) with a microchannel plate. A prototype (MPM 5 × 5)*) was tested at CERN [2].

The anode of such a detector was made of a square matrix of 5 × 5 elements, 2.5 × 2.5 mm$^2$ each. We had hoped, at that time, that a tube of about 40 × 40 mm with the same pixel size could be obtained, which would have been placed at the position of the primary image, and these considerations led us to choose an

*) Made by LEP, Paris, France.

effective focal length of 1 m for the first stage. Had such a solution been satisfactory, the second stage, consisting of the transfer lens and the field lens matrix, would not of course have been necessary.

The prototype tested, which had a glass window and a bialkali photocathode, exhibited very interesting features, in particular for the detection of single photoelectrons [2], and we had hoped that for a larger tube we would have

$$50 < A < 100 \text{ cm}^{-1}$$

with therefore

$$22 < N < 44 \text{ photoelectrons} .$$

Unfortunately, during these tests it turned out that the cathode was rapidly destroyed by ionic bombardment, and the lifetime of the tube was therefore considered too short.

The alternative solution, which has been adopted, is the use of a matrix of Hamamatsu R760, 14 mm diameter fused-silica window phototubes with a bialkali photocathode. Extensive tests made on these tubes [2] have shown interesting performances. The relative quantum efficiency of our sample of tubes is shown in fig. 4.

Such a solution requires a magnification of the primary image, which covers a field of 55 mm, in order to match it to the physical size of the phototubes and associated magnetic shielding tubes, i.e. 16 mm diameter. A matrix of 11 × 11 of such phototubes has been used for the tests reported here, and the primary image is focused by the transfer lens onto a matrix of 11 × 11 square lenses. Each of these lenses, acting as a field lens, images the exit pupil of the transfer lens onto a phototube. The sides of these lenses are not chamfered, and as they are pressed one against the other there is no dead space between them. Therefore all the light received by each of them is collected on the 9 mm diameter photocathode, except for the transmission losses, which have been minimized by the use of the same antireflection coating treatment as was used for the other optical elements of the counter. These fused-silica lenses have a focal length of 100 mm and require well-polished but not high-precision surfaces.

## 7. EXPERIMENTAL CONDITIONS

### 7.1 Set-up

The counter was tested in a 50 GeV/c positive beam at the CERN SPS, containing 65% $\pi^+$, 32% p, $\sim$ 4% $K^+$, and $\sim$ 0.02% d.

Simplicity and cost considerations led us to fill the counter with $N_2$, although for a better chromatic correction a He-Ne mixture would have been better. The gas refractive index was monitored by a fully immersed interferometer-refractometer with a digital read-out and a least-count value of $5 \times 10^{-7}$. The gas pressure could be adjusted to tune the counter to the spot-focusing condition for different values of $\gamma_0$ corresponding to $\pi$, K, p, or d. However, the chromatic correction, which depends on $\gamma_0$, was not changed as this would have implied the inconvenience of a modification of the gas composition. Figure 5 shows how the radius of the ring varies with the gas refractive index for $\pi$, K, and p.

The beam was magnetically focused onto a small region with a $5 \times 5$ mm$^2$ cross-section located at the centre of curvature T of the first mirror $M_1$ (where the target would normally be situated). Two scintillators ($S_1$ and $S_2$) along the counter axis, 4.5 m apart and having a cross-section of $3 \times 3$ mm$^2$, were used to define particle trajectories with an impact parameter $a \leq 1.5$ mm and a divergence of 0.67 mrad maximum. Another set of smaller scintillators was added during a second phase of the run in order to reduce the angular divergence of the particles (see section 8).

The base of each phototube (fig. 5) consisted of a voltage divider, designed by the manufacturer and modified according to our requirements (essentially an increase in the potential between photocathode and first dynode in order to improve the quantum efficiency [2]).

The high voltage on each phototube was adjusted with a potentiometer so that all phototubes were operating at the same point on the plateau of the characteristic curve. The adjustments were made using a Xe flash tube and a Wratten optical filter selecting the 360 nm Hg line. The main high voltage was set to 1400 V for most of the tests. The power dissipated is $\sim$ 0.45 W in each base. The phototubes were connected through 50 $\Omega$ R6U cables, 50 ns long, to the input of a

LeCroy ADC 2249A. The trigger signal produced by the coincidence $S_1 \times S_2$ was used to gate each event.

The ADCs were read through CAMAC by a PDP-11.

7.2 Data recording

Three types of data recordings and displays could be obtained.

i) A pattern showing which phototubes were fired by a single event (figs. 6, 7 and 8). In these figures, as in the following, F represents the experimental refractometer reading of the index of refraction of the gas and $n - 1 = F \times 5 \times 10^{-7}$.

ii) A pattern produced by the accumulation of many events where, on the display, each cell is represented by a square, the size of which is proportional to the number of times it has been hit by at least one photoelectron (hit pattern).

iii) A pattern produced by the accumulation of many events, as above, but the square size is proportional to the sum of the pulse amplitudes measured by the corresponding ADC (pulse pattern).

A recording of these data on tape could also be obtained on request.

A few examples of such patterns are shown in figs. 9 and 10. It was also possible to do a direct image analysis by a remotely controlled translation of the field lens in a direction parallel to the symmetry plane of the system. This movement produces a scanning of the phototube array by the image. By selecting a row of three phototubes along a direction perpendicular to the displacement, the situation was the same as if the image was scanned through a slit 4.8 cm long and 1.6 cm wide, corresponding to an angular definition of 2.4 and 0.8 mrad, respectively. The intensity profile produced by an accumulation of events was determined by recording the total number of hits in this "slit" as a function of the transfer lens position. Such a method has also been used to focus the image produced on the matrix by the transfer lens. This is achieved when the intensity profile is the sharpest (fig. 11).

## 8. RESOLUTION OF THE DETECTOR

Distinctions must be made between the various factors affecting the velocity and angular resolution of this detector.

a) The optical resolution

The performance of the optics limited by the residual aberrations, and the quality of the optical elements, are ultimately the factors limiting the resolution of the detector and will be discussed in detail (see section 8.1).

b) The matrix resolution

Discrete and relatively large phototubes limit the resolution if the equivalent focal length of the system is not sufficiently large. For a given matrix it is always possible to trade matrix resolution against the angular acceptance of the detector simply by changing the magnification of the transfer lens. If instead of phototubes a high-resolution, 10- to 20-line pairs/mm image intensifier was used at the primary image plane, all the information given by the optics would be resolved.

c) The beam divergence

The beam divergence has a very small effect in the present case [1], and we have checked (fig. 12) that no effect is visible when the particle divergence is increased in steps up to the 3.2 mrad limit set by our restricted matrix size.

d) The target size

It has been demonstrated [refs. 1 and 6] and is shown here (fig. 13) that for particles emitted from a point at a small distance from the axis, the image produced departs from a sharp spot or a true circle. We know that the light rays fall on fourth-order curves in the image plane. An appropriate fit through the image could in such cases provide not only the $\gamma$ and the divergence angle of the particle but also its azimuthal angle and its impact parameter, as can be seen from the equations of the image [1]. These fits are possible only on individual events and with a precision depending on the number of recorded photoelectrons.

For this test run we have not tried to achieve such a degree of sophistication, but we observe that with the target size considered here and for an accumulation of events this effect was similar to that of a 0.22 mrad beam divergence corresponding to the acceptance when counters $S_1$ and $S_2$ were of 1 mm diameter.

e) The multiple scattering of the particle in the gas radiator

At 50 GeV/c and with $N_2$ as a radiator the gas pressure is about 2.2 atm; and the multiple scattering angle calculated for these conditions amounts to $(\Delta\theta^2)^{\frac{1}{2}} \sim 0.07$ mrad and is negligible compared to the other factors affecting the precision.

## 8.1 Calculated optical resolution

Our ray-tracing simulator has given the spot size for $\gamma_0 = \infty$ and the ring widths at $\gamma = 50$, evaluated at the primary- and secondary-image planes produced by the first stage and the complete optical system, respectively. Tables 5 and 6 give the aberration data for the two cases of interest, i.e. the spot focusing and the ring focusing. Aberrations at the first focus and at the second focus after the transfer lens are given, with the corresponding velocity resolution of the SFD.

## 8.2 Direct tests on the optical resolution of the first-stage optics

Direct observation of the image of a monochromatic point object produced by the optical system tested by autocollimation on a bench has shown a spot size $< 0.3$ mm diameter, with some flares. Moreover, the transfer lens scanning method has also shown some astigmatism in the image. We believe that this is due to a slight sagging of the inclined plane mirror $M_p$ (see section 5).

## 8.3 Beam tests on the optical resolution of the complete optical system

With $N_2$ as a filling gas for the counter, we know that spot focusing and chromatic compensation are obtained simultaneously for $\gamma_0 = 79.6$ (see section 2.1). When working at a momentum of 50 GeV/c and adjusting the pressure to obtain spot

focusing for protons ($\gamma_0 = 53$), kaons ($\gamma_0 = 101$), or pions ($\gamma_0 = 360$), the chromatic dispersion is never correctly compensated (fig. 14). For example, when $\gamma_0 = 53$, the system is under-compensated, and this gives rise to an angular chromatic spread of the image of $\sim 0.14$ mrad according to eq. (17). When $\gamma_0 = 360$, the system is over-compensated and the angular spread is then $\sim 0.1$ mrad.

The optical resolution may be studied using the transfer lens scanning method. Figure 11 shows an example of the intensity profile obtained with accumulated events. The central peak is produced by the spot image of protons, whereas the two other peaks correspond to the accumulated rings produced by pions. A deconvolution of the intensity profile exploration by the "phototube slit" is made simply by measuring the slope of the distribution. It is then necessary to distinguish, in the result, the component due to the particle divergence in order to find the angular spread of the image produced by the optical aberrations alone. We have taken the pessimistic assumption and have added these two components quadratically. We have considered the results of the analysis on the secondary image and scaled them to the primary image plane where 1 mrad is equivalent to 1 mm. We then find an optical over-all angular spread of $\sim 0.320$ mrad for a ring image and 0.40 mrad for a spot. From this we can derive the expected velocity resolution due to the optical aberration, by a differentiation of the basic Čerenkov relation

$$\frac{\Delta\beta}{\beta} = \text{tg}\ \theta_0\ \Delta\theta\ , \tag{20}$$

In our case $\text{tg}\ \theta_0 \sim \theta_0 = 35$ mrad and $\Delta\theta \leq 0.32$ mrad for a ring image. The spot image is not symmetric and is probably overestimated, counter $S_1$ not being set properly at the target position in the vertical plane.

We have then

$$\Delta\beta_{\text{optics}} \leq 11.2 \times 10^{-6}\ . \tag{21}$$

However, it has been found [3] that a good separation is obtained when the velocity difference between particles is at least three times the resolution. In this

case $\Delta\beta_{optics} \sim 34 \times 10^{-6}$, and the maximum momentum for $\pi$-K separation will be $\sim$ 80 GeV/c and for $\pi$-p separation $\sim$ 160 GeV/c.

In the present case, however, one must also take into account the effect of the matrix resolution on these performances.

It has been found by Monte Carlo simulation that a perfect circle can be determined with an error of ±0.09 pixel on the radius (when the radius is larger than one pixel). It is then possible to estimate the error introduced in the velocity determination by the matrix resolution

$$\frac{\Delta\beta_{matrix}}{\beta} \sim 0.18 \times \text{tg}\ \theta_0 \times \Delta\theta_a \ , \tag{22}$$

$\Delta\theta_a$ being the angular acceptance of one cell:

$$\Delta\theta_a = 0.8 \text{ mrad} \ , \tag{23}$$

and then

$$\Delta\beta_{matrix} \sim 5 \times 10^{-6} \ . \tag{24}$$

We find that the limit on the velocity resolution as set by the matrix structure (with a magnification factor of ×20 for the transfer lens and a global equivalent focal length of 20 m for the detector) is about half the over-all optical resolution that we had deduced from the transfer lens scanning.

It is also possible to have a direct determination of the velocity selection of the SFD from the distribution of ring radii of fitted single events by the least-squares-fit method applied to all the hits of the pattern. In this case the divergence of each particle does not play any role. This method suffers from a serious defect. The patterns which contain one or more hits uncorrelated with the Čerenkov ring can be badly fitted, leading to large tails in the histograms. Clearly a more sophisticated data handling is required. An effective ring radius resolution of $\sim$ 0.5 ± 0.1 pixel (figs. 15, 16, and 17) was found. The observed velocity resolution for fitted single events is then

$$\frac{\Delta\beta_{tot}}{\beta} \sim 14 \times 10^{-6} \ . \tag{25}$$

This shows

- a fairly good agreement between the two methods of measurement ("slit analysis" and pattern analysis);
- a fairly good agreement also with our theoretical predictions;
- a justification for the choice of 20 m for the equivalent focal length, because the resolution is limited mostly by the optical aberrations, and to some extent by the matrix structure.

Figure 18 shows the fitted radii of pions, kaons and protons of 50 GeV/c, for different values of the index of refraction of the gas.

The relativistic factor $\gamma$ of a particle can be deduced from the index of refraction of the ring radius in pixels by the approximate formula:

$$\gamma = \left[2(n - 1) - (\theta_0 \pm R\Delta\theta_a)^2\right]^{-\frac{1}{2}} . \qquad (26)$$

In our case $(n - 1) = 5 \times 10^{-7} \times F$, $\theta_0 = 34.25 \times 10^{-3}$, $\Delta\theta_a = 8 \times 10^{-4}$; in this formula, F is the refractometer reading. Therefore

$$\gamma = \left[F \times 10^{-6} - (34.25 \times 10^{-3} \pm 8 \times 10^{-4} \times R)^2\right]^{-\frac{1}{2}} . \qquad (27)$$

## 9. LIGHT YIELD

The most important characteristics of this detector, and indeed the main reason for our tests in a beam, is probably the actual average number $\bar{N}$ of detected photoelectrons per single event. It is possible to be confident enough in the optical computations and in the lens-making techniques to predict with a high accuracy the optical resolution of a spot-focusing detector, but the usefulness of such a detector is directly linked to the number of bits of information obtained per event, i.e. the number of photoelectrons detected by the complete system, electronics included.

It is of great interest to evaluate experimentally the average number $\bar{N}$ of photoelectrons produced per singly charged particle, and to compare it with the

expected values derived by computation. Our method is based on the fact that there is a close relation between the number of cells triggered by an event, the radius of the ring, and the number of photoelectrons produced. A Monte Carlo simulation has shown how these parameters are related (fig. 19). If for a sample of events we know the average radius and the average number of cells hit, it is then possible to derive the average number $\bar{N}$ of photoelectrons produced per event, and therefore the average value of A for the R760 phototubes, when the optical transmission T of the optics is known. This study, carried out on two samples of pions obtained with two different refractive index settings, is shown in table 7.

There is an independent experimental determination of the light yield obtained by the transfer lens scan across a ring image. When the gas refractive index is set at $(n - 1) = 748.5 \times 10^{-6}$, the pions in the beam with $\gamma = 360$ produce a ring image of 4.3 pixels radius. The photoelectrons are spread along the 27-pixel-long circumference. Therefore a phototube along this circumference, when hit, receives an average signal corresponding to one photoelectron for this event. When scanning with the transfer lens and looking at the signal of the central phototube ($PM_0$) of the matrix, it is found that the efficiency of the triple coincidence

$$\eta = \frac{PM_0 \times S_1 \times S_2}{S_1 \times S_2} \qquad (28)$$

differs appreciably from 1 and is only $0.70 \pm 0.05$ when $PM_0$ is set on the ring image for pions. But it becomes $\sim 1$ on the central spot, produced by protons ($\gamma = 53$). We do not know the exact ratio of protons to pions in the beam; but we can measure it, as well as the average number of photoelectrons $\bar{N}$ produced by the pions, by repeating the scan with the "phototube slit" (see section 8.3). In this case the efficiency reaches nearly 1 on the pion ring. From a comparison of these two efficiencies and knowing that $n = (1 - e^{-\bar{N}})$, we can deduce that we have a signal on the central phototube of $1.2 \pm 0.2$ photoelectron per event. However, we cannot consider this value as typical for all the phototubes, since we tested them (fig. 4) and installed the best ones at the centre of the matrix. Compared

with the average value of the distribution of the phototube efficiencies, this one is 1.14 times more efficient. Therefore we can estimate that the matrix receives, on the average, for the average-quality phototube, $\bar{N} = 28.4 \pm 6$ photoelectrons/event. Taking the average of the two different measurements, we obtain $\bar{N} = 24.6 \pm 3.6$ with admittedly large uncertainties. This value is very similar to the one used in the DISC design [3].

We know that the ring radius of a particle with a $\gamma$ value different from the tuning value $\gamma_0$ depends only on the quantity $|\gamma - \gamma_0|$, and we have studied rings of the same radius produced by particles with $\gamma_1 > \gamma_0$ and with $\gamma_2 < \gamma_0$ but such that $(\gamma_1 - \gamma_0) = (\gamma_0 - \gamma_2)$. We have found that in such cases there is 30% difference in the $\bar{N}$ value. This fact may provide a way of removing ambiguities in the determination of the $\gamma$ of the particles.

## 10. OPTICAL TRANSMISSION AND FIGURE OF MERIT OF THE PHOTOTUBES

### 10.1 Optical transmission of the SFD

The optical transmission losses through the system are far from negligible, as the Čerenkov light is reflected by three mirrors and is transmitted through 10 interfaces between $SiO_2$ and gas, and 14 interfaces between $SiO_2$ and $H_2O$. Moreover, the average path lengths in $SiO_2$ and in $H_2O$ are 150 mm and 33 mm, respectively.

We have measured the transmission of the system at the 365 nm Hg line, which is an approximation to the effective Čerenkov spectrum peak of 350 nm as detected by the phototubes. For the first-stage optics alone, which would be the only part required if a multianode phototube or an image intensifier was used, $T_1$ is $\geq 0.405$. Practical difficulties in this measurement, taken over an 8 m light path, are such that we can quote only a lower limit:

for the transfer lens: $T_2 = 0.90$

for the field lenses in front of the phototubes: $T_3 = 0.946$.

The total measured transmission of the system as it was used during our test is therefore $T = T_1 \times T_2 \times T_3 \geq 0.345$.

It is interesting to check the consistency of these measurements.

For the transfer lens the transmission is given by the product of three terms. One is the transmission of a fused-silica lens coated on both sides, like the field lenses, $T_3 = 0.946$. This transmission is about 1% smaller than that found by computation. The second term is the transmission of 14 $SiO_2$-$H_2O$ interfaces, $T_4 = 0.972$; and the third term the transmission of 16 mm of $H_2O$, $T_5 = 0.995$.

Therefore we expect that $T_2 = 0.91$, which is in good agreement with the measured value.

For the first-stage optics alone we have three mirrors. For each of these we have measured a reflection coefficient of 0.83, and six $SiO_2$ gas interfaces (equivalent to three coated $SiO_2$ lenses) and two $SiO_2$-$H_2O$ interfaces. We therefore expect $T_1 = 0.48$ leading to $T = 0.41$. The agreement between the measured value and the computed one is considered to be rather good if we take into account the practical difficulties that have to be faced for such delicate measurements.

10.2 Figure of merit of the phototubes R760

It is interesting, notwithstanding the limited accuracy of these measurements, to evaluate the figure of merit A* of the R760 photomultiplier from eq. (19):

$$A^* = \frac{\bar{N}}{T \times L \times \theta_0^2} \,. \tag{29}$$

With $A = A^* \times T$, and $\theta \sim 38.44$ mrad, for pions producing a ring of 4.3 pixels diameter, T (the optical transmission of the complete system) is > 0.345, and we know it may be as large as 0.41, L = 360 cm, $N = 24.6 \pm 3.6$.

We then find, according to the value of T,

$$A^* \sim 134 \pm 20$$

or

$$A^* \sim 113 \pm 17 \ .$$

These results confirm the relatively good quality of the phototubes.

## 11. UTILIZATION OF A SPOT-FOCUSING DETECTOR

The detector can be run in two modes. One mode is the spot focusing for at least one particle emitted in an interaction at a given $\gamma_0$. The electronics recognizes the presence of a spot extending over very few adjacent pixels and containing N photoelectrons. The position of the spot on the matrix is a measurement of the angle of emission, and the mere presence of a bright spot is the proof that the particle has $\gamma_0$ for its relativistic factor. If the momentum p of the particle is known from its magnetic rigidity, these three parameters define the mass M, the longitudinal momentum $p_L$ and the transverse momentum $p_T$ of the particle. These data provide a very useful indicator which could be used to trigger the data acquisition of the event. Clearly this requires that the N photoelectrons produced in a cluster be efficiently recognized over the inherent noise of the photodetector, and that spurious triggers occur only at a negligible rate. We have tested this possibility in searching for deuterons in the beam. Figures 20 and 21 indicate how these particles have been detected and could easily have been used as trigger particles.

The detector can be also used in another mode when the particles of interest do not necessarily produce a spot but a circle. The pattern recognition and reconstruction of these circles, which may be too slow for trigger purposes, call for a sufficiently large number N of photoelectrons per event. However, this number does not need to be so large as to produce a hit on nearly all the pixels which correspond to the circle. It can even be said that such an abundance of photoelectrons rather than improving the reconstruction would only make the analysis of multiparticle events more complicated. Experience will tell us the

suitable values for N, but it can be guessed that for a satisfactory performance it will lie between 10 and 30.

However, we do not underestimate the difficulties we will find in multiparticle events when more than one circle per event has to be recognized and reconstructed. This is a wide subject that we cannot discuss in this article, which is devoted to the performance of the detector rather than to the way in which the results should be exploited. Such a question can only be tackled when enough experience has been gained in the practical use of the detector. We will limit ourselves to illustrating the problem, using one particular example. We have tested the possibility of disentangling multiparticle events such as the one shown in figs. 22 and 23. Using an inversion, we transform the circle of the hit pattern into an easily recognized straight line when the pole is on a circle. Figure 24 shows the inverted pattern and fig. 25 the identified circles. They correspond to particles of $\gamma = 47.8$ or $\gamma = \infty$, and $\gamma = 48.4$ or $\gamma = \infty$. The four unidentified hits in the circles can correspond to a circle of about 1.5 pixel in radius.

If they are the signature of a beam proton, a pulse-height analysis could prove that this is due to the concentration of the light on a few pixels. Tentatively we can interpret this event as two electrons produced by a beam proton.

## 12. CONCLUSIONS

All these results show that a spot-focusing detector, as described in the original article [1], can indeed be built, and its measured performances agree closely with the design data.

The main reason for the optical complexity of the present device lies in the uncertainty which existed at the design stage concerning the photodetection system. Moreover, the actual performances, particularly the limited angular acceptance, are the result of a deliberate decision to build a test instrument and to minimize its cost. However, this detector, as it is, can be used as a convenient beam particle identifier, since we have shown that it can tag three different types of

particles simultaneously in a non-parallel beam, unlike a DISC counter [3,4] which requires a parallel beam, and this feature may save beam transport lenses and space.

An SFD has the same advantages as a DISC: very short output pulses (a few nanoseconds), very high counting rate capability ($\geq 10^7$/sec), immunity to low-velocity background particles, and high-velocity resolution ($10^{-6}$ can be achieved). It has also specific advantages over a DISC: 100% detection efficiency thanks to its average of $\sim$ 25 photoelectrons per event, which do not have to be collected through a narrow diaphragm as in a DISC. (In the latter a certain fraction of them are lost owing to the spread of the ring image, and this spread is larger than the diaphragm, whose width is fixed by the tolerance on the velocity and the divergence of the particle.) Moreover, the present SFD has multiparticle detection ability and very good spatial resolution. It is an interesting forward detector which can produce a trigger on the passage of a particle with a preset $\gamma$ value, at a given angle.

A new project would of course use single-stage optics, instead of two, with a purely refractive axiconic objective giving, in one step, the final equivalent focal length. In this case this objective would be crossed only once by the light, and there would be no need for a transfer lens. The total light transmission coefficient could be raised to at least 0.62. One could even make use of an axiconic lens identical to the present one. In this case the nominal Čerenkov angle would be twice as small, i.e. 17.5 mrad, giving a better velocity resolution, and therefore such a counter could work in the range 100-300 GeV/c. The length of this counter could then be doubled in order to produce nearly the same global light yield. The design could also include a larger free space between the target and the counter body so as to allow for the installation of a vertex detector and a magnet. Working at about atmospheric pressure with a gas mixture such as He and $N_2$ and the refractive index being measured with an internal interferometer-refractometer, such a detector would introduce a minimal amount of material in the particle path. We think that an SFD can be the best Čerenkov detector for

most of the cases where the interaction region is a target of limited size such as an external target in secondary particle beams, or the intersecting region of storage rings where topological problems associated with the presence of vacuum tubes will limit the detection capabilities along the beams axis.

Acknowledgements

This SFD project has been made possible by the support of P. Falk-Vairant, E. Gabathuler and E. Picasso, of the CERN Experimental Physics Division, and P. Zanella of the Data-Handling Division; A. Muller, from CEN Saclay, and many other people have contributed to its success. Drs. E. Lesquoy and S. Zylberajch have been responsible for the data acquisition and the data analysis. Their contribution merits our appreciation. We would like to acknowledge the skill and the patience of J. Mortleman and J. Thomson (from Optical Surfaces, Ltd.) who polished the axicon and the aspherical mirror. We want also to thank C. Nichols and his staff for the careful grinding and the antireflection coating of the optical elements. Drs. Brian Powell and Jayanti Dharma Teja are especially thanked for their careful reading of the manuscript and their constructive remarks.

## REFERENCES

[1] M. Benot, J.M. Howie, J. Litt and R. Meunier, Nucl. Instr. and Meth. 111 (1973) 397.

[2] R. Meunier and A. Maurer, IEEE Trans. Nucl. Sci. NS-25, N1 (1978) 528-531.

[3] M. Benot, J. Litt and R. Meunier, Nucl. Instr. and Meth. 105 (1972) 431.

[4] J. Litt and R. Meunier, Annu. Rev. Nucl. Sci. 23 (1973) 1.

[5] A. Bouwers, Achievements in optics (Elsevier, New York, 1950), p. 16 *et seq.*

[6] M. Benot and J.M. Howie, Evaluation of the image in a spot focusing Čerenkov counter, CERN Data-Handling Division Report DD/73/1 (Feb. 1973), unpublished.

Table 1

Gas index and chromatic dispersion as a function of $\gamma_0$

| $\gamma_0$ | $(n_g - 1) \times 10^6$ | $\nu_g$ |
|---|---|---|
| 10 | 5612.50 | 167.67 |
| 20 | 1862.50 | 55.64 a) |
| 40 | 925.60 | 27.63 |
| 50 | 812.98 | 24.27 |
| 80 | 690.99 | 20.63 b) |
| 100 | 662.85 | 19.79 |
| 200 | 625.32 | 18.67 |
| 500 | 614.81 | 18.36 |
| $\infty$ | 612.81 | 18.30 |

a) pure He

b) pure $N_2$

Table 2

Spot-focusing detector optical specifications

| Surface | Medium | Position (mm) | R curvature or angle (mm) (mrad) |
|---|---|---|---|
| Sph. mirror | Gas | 4000 | -4000 |
| Plano | Gas | 45.30 | |
| Plano | $SiO_2$ | 39.10 | 137.0 |
| Conical | $H_2O$ | 39.10 | |
| Plano | $SiO_2$ | 2.71 | |
| Asph. mirror | Gas | -5.40 | -1333 a) |
| Plano | Gas | 2.71 | |
| Conical | $SiO_2$ | 39.10 | 137.0 |
| Plano | $H_2O$ | 39.10 | |
| Plano | $SiO_2$ | 45.30 | |
| | Air | | |

a) $\varepsilon = 0.6$, $\varepsilon' = -24$, see section 3.2.

Table 3

Transfer lens optical specifications

| Medium | Position (mm) | R curvature (mm) |
|---|---|---|
| Air | 0 | -58.65 |
| $SiO_2$ | 4 | -50.87 |
| $H_2O$ | 4 | 28.57 |
| $SiO_2$ | 5.85 | 26.72 |
| $H_2O$ | 13.85 | 72.35 |
| $SiO_2$ | 23.85 | -72.35 |
| $H_2O$ | 23.85 | 72.35 |
| $SiO_2$ | 33.85 | -72.35 |
| $H_2O$ | 33.85 | 72.35 |
| $SiO^2$ | 43.85 | -72.35 |
| $H_2O$ | 43.85 | 72.35 |
| $SiO_2$ | 53.85 | -72.35 |
| $H_2O$ | 61.85 | -26.72 |
| $SiO_2$ | 63.7 | -28.57 |
| $H_2O$ | 63.7 | 50.87 |
| $SiO_2$ | 70.7 | 583.0 |
| Air | | |

EFL (= equivalent focal length) = 94.24 mm

BFL (= back focal length) = 85.22 mm

Table 4

Measured transmission

of the transfer lens

| Wavelength (nm) | Transmission (%) |
|---|---|
| 334 | 87.5 |
| 365 | 90 |
| 405 | 93.5 |
| 436 | 95 |
| 546 | 96 |

Table 5

Spot-focusing detector aberration data

(SFD tuned for spot, $\gamma_0 = \infty$; full angular size in mrad)

| $\tau$ | 1st focus, SFD alone | | | 2nd focus, SFD + TL | | |
|---|---|---|---|---|---|---|
| | radial (μm) | $\Delta\beta/\beta$ | tangent. (μm) | radial (μm) | $\Delta\beta/\beta$ | tangent. (μm) |
| 0 | 0.152 | $\pm 2.7 \times 10^{-6}$ | 0.152 | 0.190 | $\pm 3.3 \times 10^{-6}$ | 0.190 |
| 5 | 0.156 | $\pm 2.75 \times 10^{-6}$ | 0.156 | 0.240 | $\pm 4.2 \times 10^{-6}$ | 0.190 |
| 10 | 0.170 | $\pm 3.0 \times 10^{-6}$ | 0.190 | 0.340 | $\pm 6.0 \times 10^{-6}$ | 0.240 |
| 15 | 0.215 | $\pm 3.75 \times 10^{-6}$ | 0.230 | 0.655 | $\pm 11.5 \times 10^{-6}$ | 0.42 |
| 20 | 0.295 | $\pm 5.2 \times 10^{-6}$ | 0.270 | | | |
| 25 | 0.285 | $\pm 5.0 \times 10^{-6}$ | 0.320 | | | |

Table 6

Spot-focusing detector aberration data

(SFD tuned for ring, $\gamma_0 = \infty$; all radii and errors evaluated in mrad)

| $\gamma$ | R | 1st focus EFL = 1.0 m | $\Delta\beta/\beta$ | 2nd focus EFL = 20 m | $\Delta\beta/\beta$ |
|---|---|---|---|---|---|
| 50 | 6.25 | ±0.1 | $\pm 3.5 \times 10^{-6}$ | ±0.25 | $\pm 8.75 \times 10^{-6}$ |
| 55 | 5.125 | ±0.085 | $\pm 2.975 \times 10^{-6}$ | ±0.12 | $\pm 4.55 \times 10^{-6}$ |
| 60 | 4.25 | ±0.075 | $\pm 2.625 \times 10^{-6}$ | ±0.1 | $\pm 3.5 \times 10^{-6}$ |
| 65 | 3.65 | ±0.070 | $\pm 2.45 \times 10^{-6}$ | ±0.085 | $\pm 2.975 \times 10^{-6}$ |
| 70 | 3.15 | ±0.065 | $\pm 2.275 \times 10^{-6}$ | ±0.075 | $\pm 2.625 \times 10^{-6}$ |
| 80 | 2.35 | ±0.055 | $\pm 1.925 \times 10^{-6}$ | ±0.060 | $\pm 2.1 \times 10^{-6}$ |
| 100 | 1.5 | ±0.045 | $\pm 1.575 \times 10^{-6}$ | ±0.055 | $\pm 1.925 \times 10^{-6}$ |
| 200 | 0.39 | ±0.040 | $\pm 1.40 \times 10^{-6}$ | ±0.060 | $\pm 2.1 \times 10^{-6}$ |
| 400 | 0.12 | ±0.0425 | $\pm 1.4875 \times 10^{-6}$ | ±0.065 | $\pm 2.625 \times 10^{-6}$ |
| $\infty$ | 0 | ±0.076 | $\pm 2.66 \times 10^{-6}$ | ±0.095 | $\pm 3.325 \times 10^{-6}$ |

Table 7

Experimental evaluation of the photoelectron yield

| Average radius in pixels | Average number of hits | N photoelectrons (from the graph) |
|---|---|---|
| 3 | 13.1 ± 1.1 | 20.5 ± 3.5 |
| 4.3 | 15.7 ± 2.3 | 21 ± 5 |

Figure captions

Fig. 1 : Spot-focusing detector.

Fig. 2 : Transfer lens spot size (diameter of circle containing 100% of the light).

Fig. 3 : Transfer lens.

Fig. 4 : Distribution of the relative efficiency of the photomultipliers.

Fig. 5 : Photomultiplier wiring.

Fig. 6 : Single-pion events. Pion spot focused, $R_\pi = 0$, F = 1181.

Fig. 7 : Single events: pion $R_\pi = +3.0$ pixel
proton $R_p = -1.75$ pixel F = 1401
kaon $R_K = +1.9$ pixel

Fig. 8 : Single-pion event: F = 1524, $R_\pi = 4.7$ pixel. This ring diameter is about the maximum accepted by the present matrix.

Fig. 9 : Spot focusing of protons of 50 GeV/c: F = 1511, $R_p = 0$, $R_\pi = 4.3$ pixel. The pion circles are very visible. There are 65% of pions and only 27% of protons in the beam; the pions also produce more light than the protons because of their larger Čerenkov angle.

Fig. 10 : Ring focusing of pions. The protons in the beam have been vetoed with a threshold Čerenkov counter. $R_\pi = 4.2$ pixel, F = 1485.

Fig. 11 : Scan across the pattern with the transfer lens.

Fig. 12 : Pattern of particles making an angle $\tau = 3.2$ mrad with the SFD axis in the horizontal plane. The pattern is displaced by 4 pixels, but otherwise it is not modified. F = 1485.

Fig. 13 : Pattern of particles passing through a target of 3 mm diameter, the target being displaced from the SFD axis by

a) = 0 mm
b) = 2.5 mm
c) = 5 mm
d) = 7.5 mm

F = 1485; $R_p = 0$. The proton spot is degraded according to the SFD theory by the impact parameter, into a small circle which is not uniformly illuminated.

Fig. 14 : Spot focusing of pions at 50 GeV/c: F = 1181, $R_\pi = 0$. The beam is centred on the PM at the centre of the matrix. There are some events hitting the adjacent PM, but the pulse pattern shows that most of the light falls on this PM. The protons produce a circle of $R_p = 5.0$ pixel and nearly miss the matrix.

Fig. 15 : Distribution of individual ring radii at F = 1000.

Fig. 16 : Distribution of individual ring radii at F = 1120.

Fig. 17 : Distribution of individual ring radii at F = 1320. Note that the proton ring radii are "negative".

Fig. 18 : Radius of the ring for $\pi$, K, and p at 50 GeV/c.

Fig. 19 : Number of hits versus $\bar{N}$ for different R.

Fig. 20 : Spot focusing of deuterons, F = 2467. Deuterons form only $2 \times 10^{-4}$ of the beam. For this pattern, data have been accumulated at a beam intensity of $3 \times 10^6$ per second. The computer limited the data-taking rate to 20 events/s. The trigger selection with two threshold Čerenkov counters reduced the rate to only about $3 \times 10^4$/s. Therefore only one particle in 50 triggers can be a deuteron. The pattern shows five deuterons focused on the centre of the matrix, as can be seen from the comparison between the hit and pulse pattern. For this run the pulse pattern was recorded with a pedestal raised to 16 units. Many spurious signals appear at certain locations in the matrix. This effect is repeated for different runs, and is connected with noise at the input of the ADC.

Fig. 21 : Pulse-height spectrum of a spot focus. The central PM is displayed when the light comes from deuterons. A similar pulse-height spectrum fills only the first few channels when the selected PM forms part of a ring focus.

Fig. 22 : Multiparticle event, F = 1401, as seen on the display.

Fig. 23 : Hit pattern of the same event on the field lens matrix.

Fig. 24 : Geometric inversion of the event.

Fig. 25 : Circles obtained from the straight line fit to the inverted pattern.

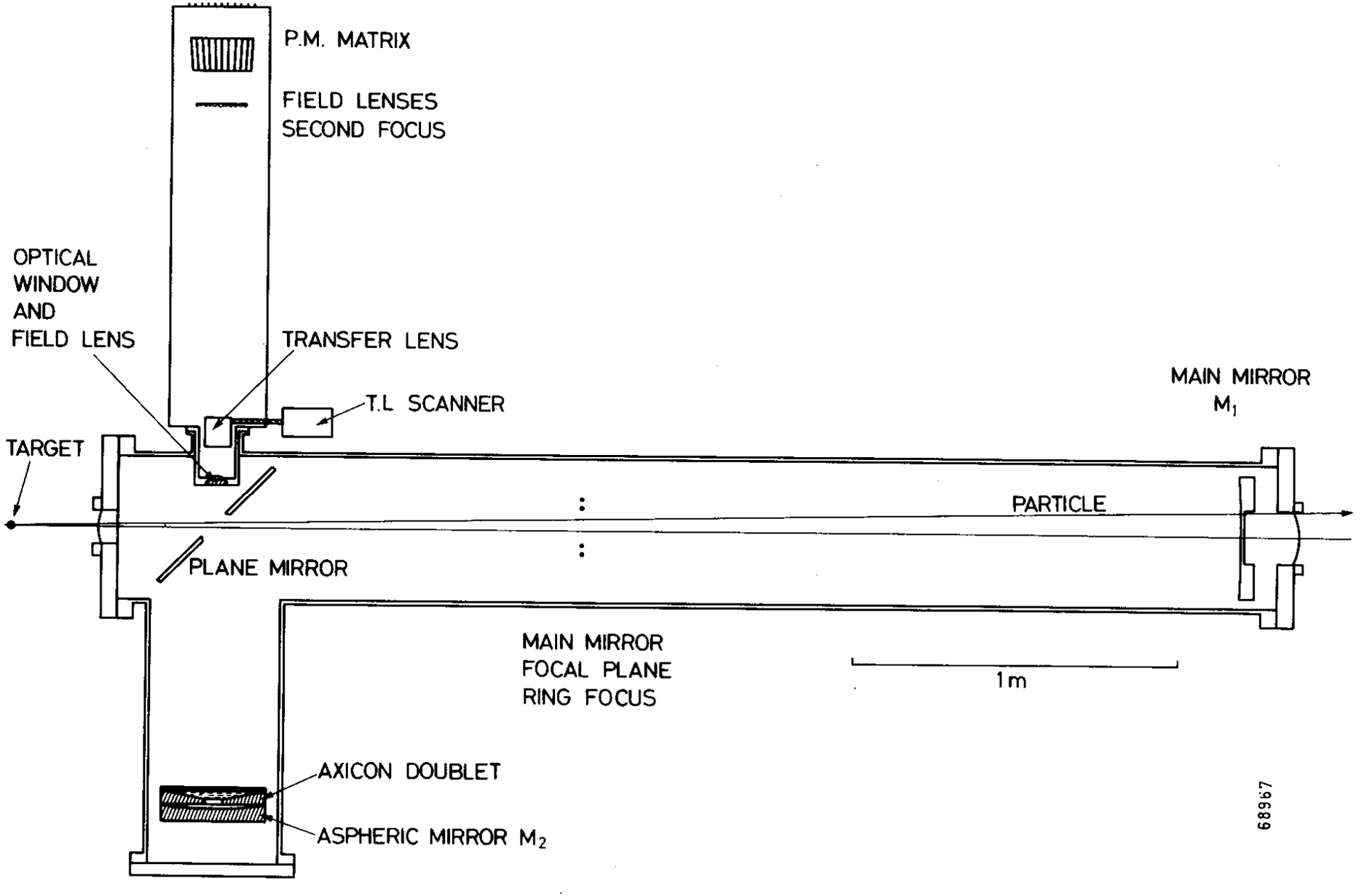
P.M. MATRIX
FIELD LENSES
SECOND FOCUS
OPTICAL
WINDOW
AND
FIELD LENS
TRANSFER LENS
T.L. SCANNER
MAIN MIRROR
$M_1$
TARGET
PARTICLE
PLANE MIRROR
MAIN MIRROR
FOCAL PLANE
RING FOCUS
1m
AXICON DOUBLET
ASPHERIC MIRROR $M_2$
68967

Fig. 1

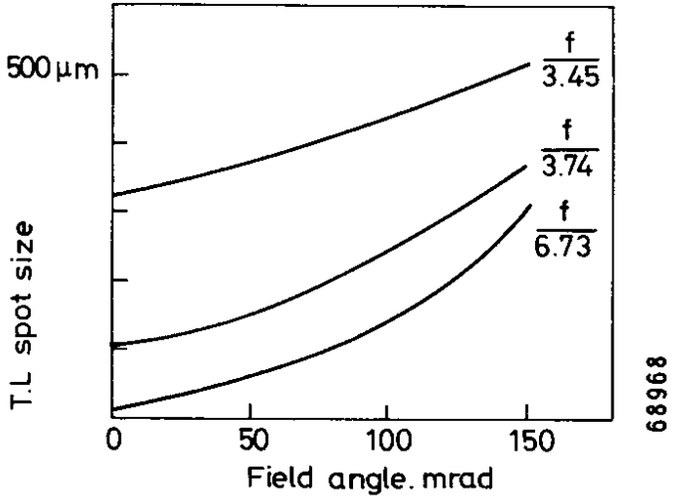
500 µm
T.L spot size
f/3.45
f/3.74
f/6.73
0
50
100
150
Field angle. mrad
68968

Fig. 2

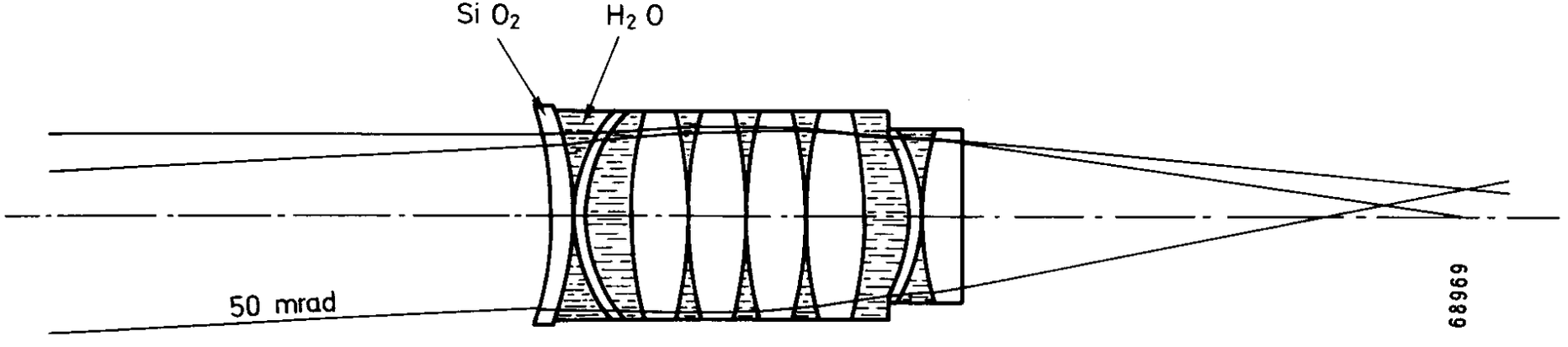
Si O2
H2 O
50 mrad
68969

Fig. 3

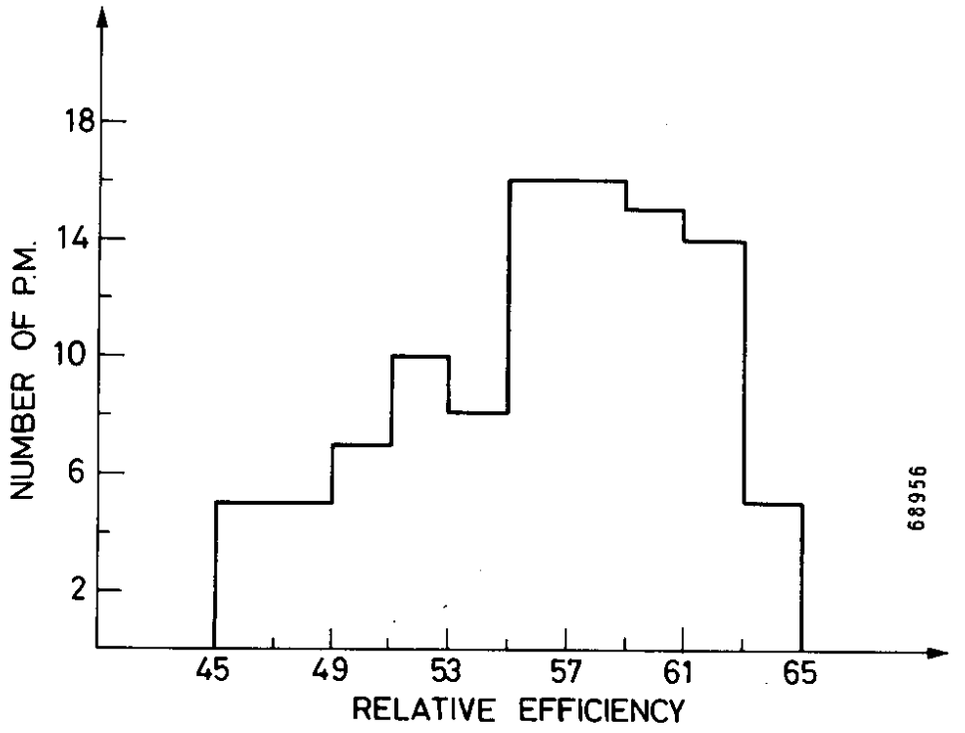
NUMBER OF P.M.
18
14
10
6
2
45
49
53
57
61
65
RELATIVE EFFICIENCY
68956

Fig. 4

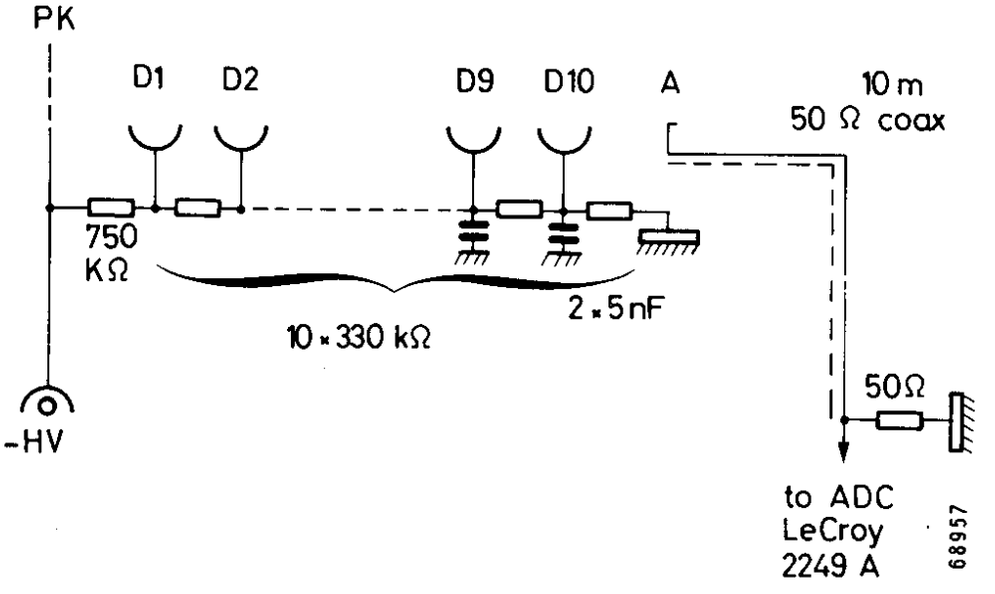
PK
D1
D2
D9
D10
A
10 m
50 Ω coax
750
KΩ
10 × 330 kΩ
2 × 5nF
-HV
50Ω
to ADC
LeCroy
2249 A
68957

Fig. 5

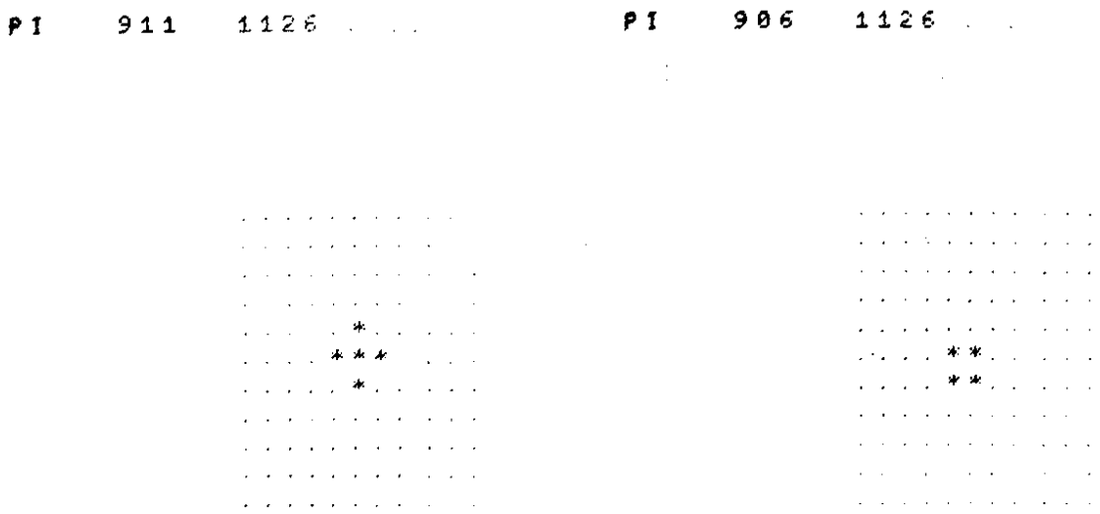


Fig. 6

PI 1001 1126

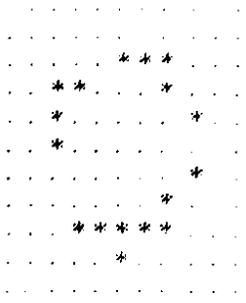

a)

PI 900 1127

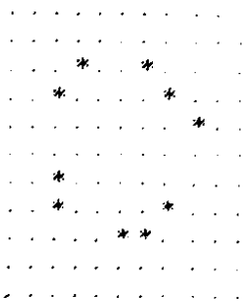

b)

P 67 59

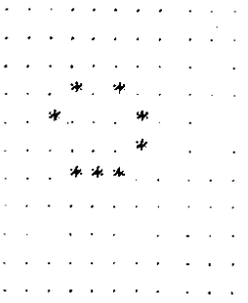

c)

K 885 71

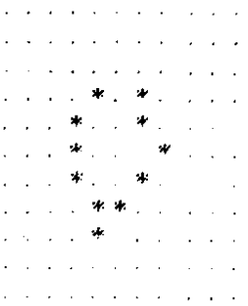

d)

Fig. 7

PI 886 1083

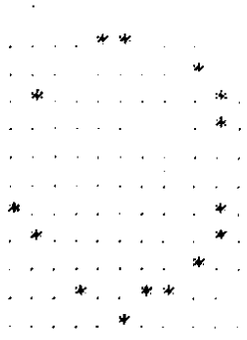

Fig. 8

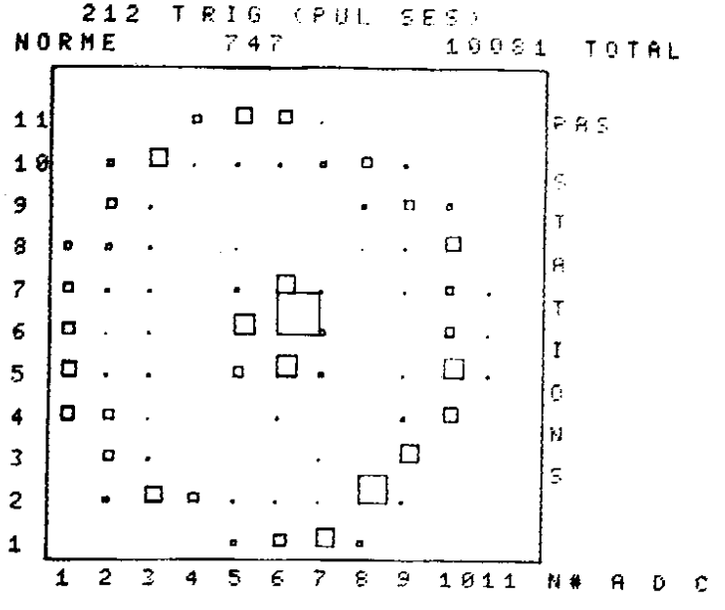
212 TRIG (PULSES)
NORME 747 10081 TOTAL
PAS
STATIONS
1 2 3 4 5 6 7 8 9 10 11 N# A D C

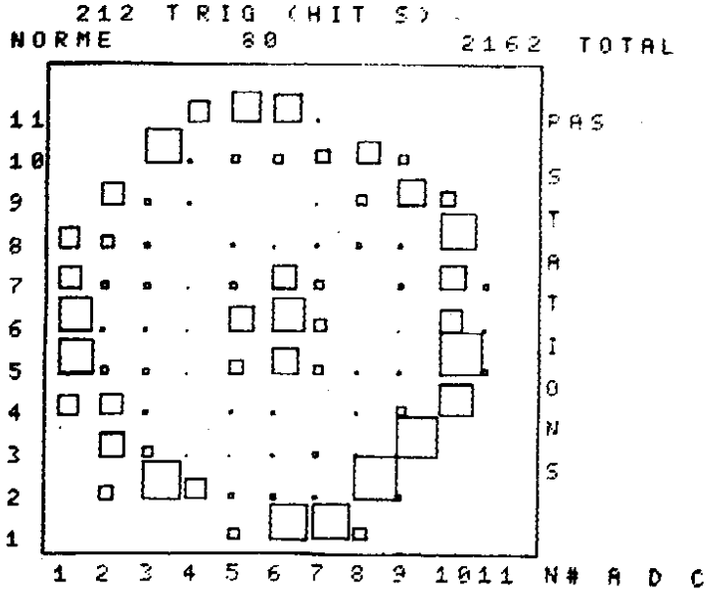
212 TRIG (HITS)
NORME 80 2162 TOTAL
PAS
STATIONS
1 2 3 4 5 6 7 8 9 10 11 N# A D C

Fig. 9

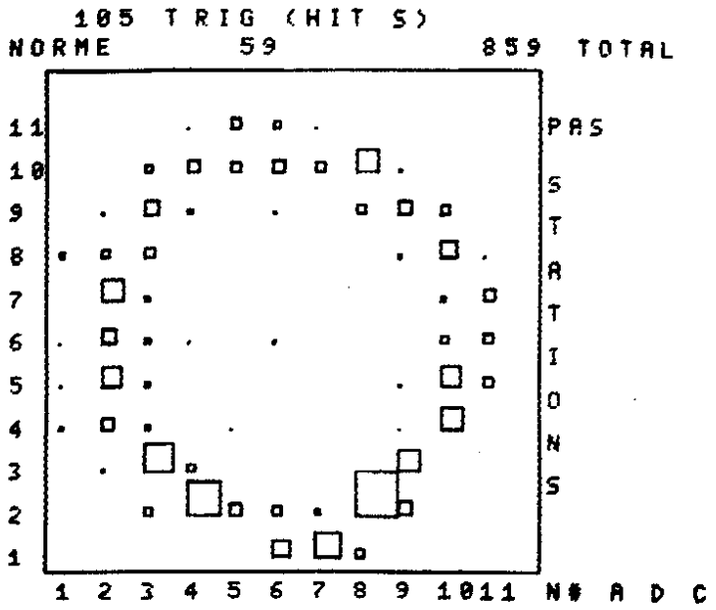
105 TRIG (HIT 5)
NORME 59 859 TOTAL
PAS
STATIONS
11
10
9
8
7
6
5
4
3
2
1
1 2 3 4 5 6 7 8 9 10 11 N# A D C

Fig. 10

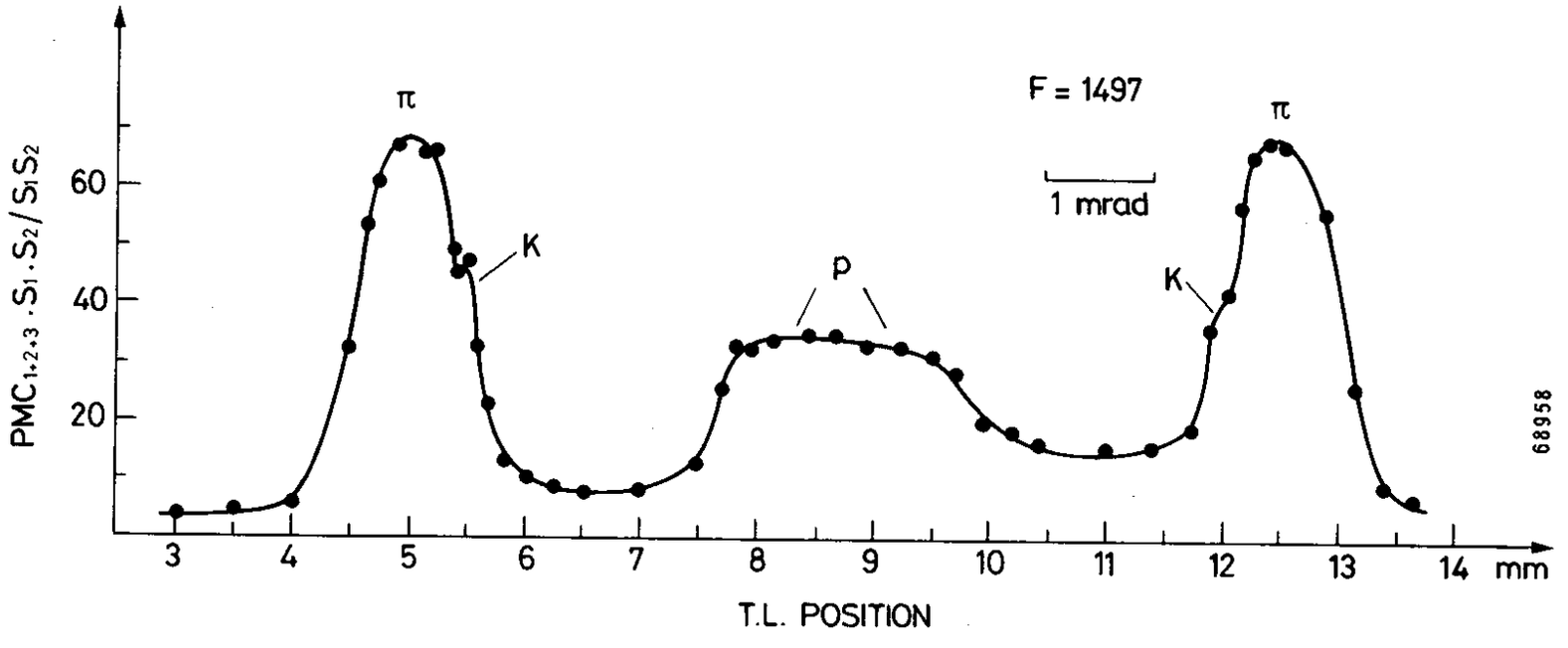
F = 1497
1 mrad
π
K
p
π
K
PMC1+2+3 · S1 · S2 / S1S2
60
40
20
3
4
5
6
7
8
9
10
11
12
13
14 mm
T.L. POSITION
68958

Fig. 11

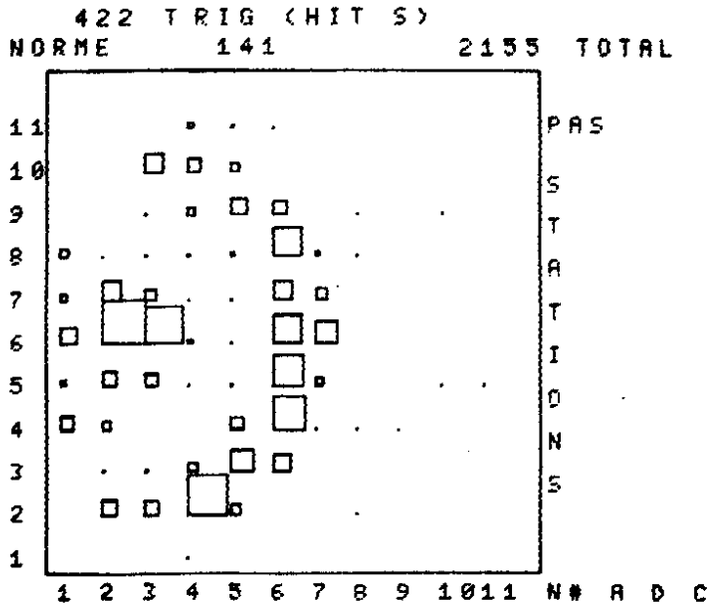
422 TRIG (HIT S)
NORME 141 2155 TOTAL
PAS
STATIONS
11
10
9
8
7
6
5
4
3
2
1
1 2 3 4 5 6 7 8 9 1011
N# A D C

Fig. 12

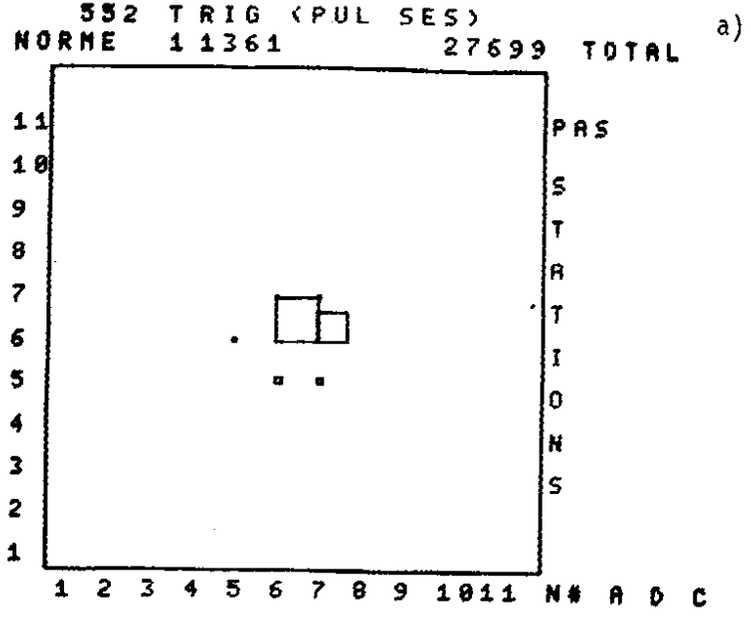
552 TRIG (PULSES)
NORME 11361 27699 TOTAL
a)
PAS
STATIONS
1 2 3 4 5 6 7 8 9 10 11 N# A D C

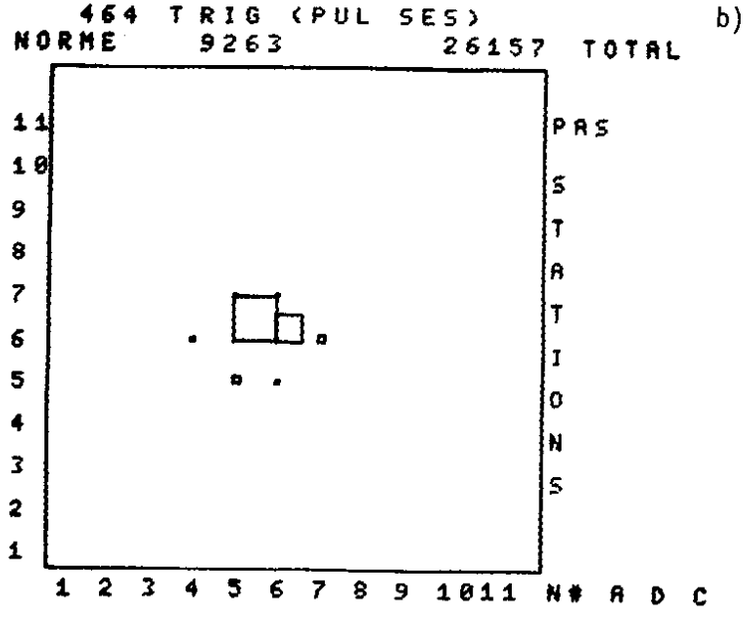
464 TRIG (PULSES)
NORME 9263 26157 TOTAL
b)
PAS
STATIONS
1 2 3 4 5 6 7 8 9 10 11 N# A D C

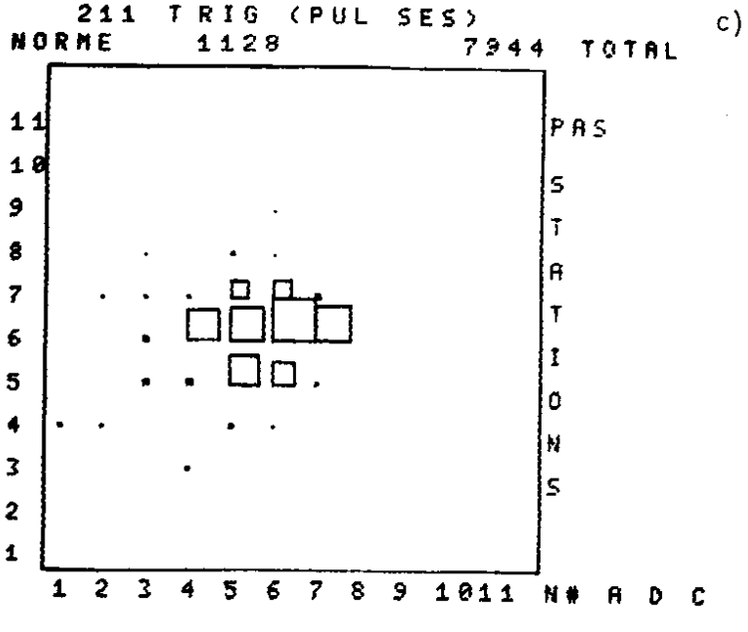
211 TRIG (PULSES)
NORME 1128 7944 TOTAL
c)
PAS
STATIONS
1 2 3 4 5 6 7 8 9 10 11 N# A D C

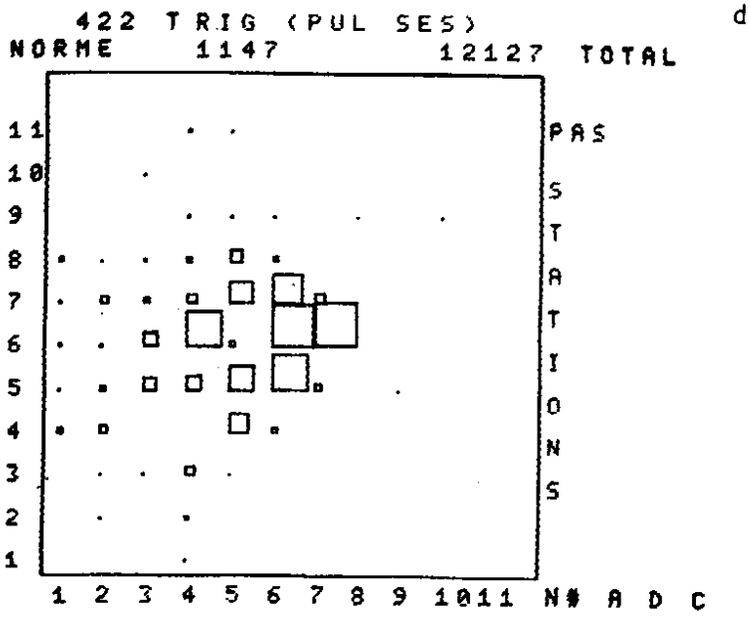
422 TRIG (PULSES)
NORME 1147 12127 TOTAL
d)
PAS
STATIONS
1 2 3 4 5 6 7 8 9 10 11 N# A D C

Fig. 13

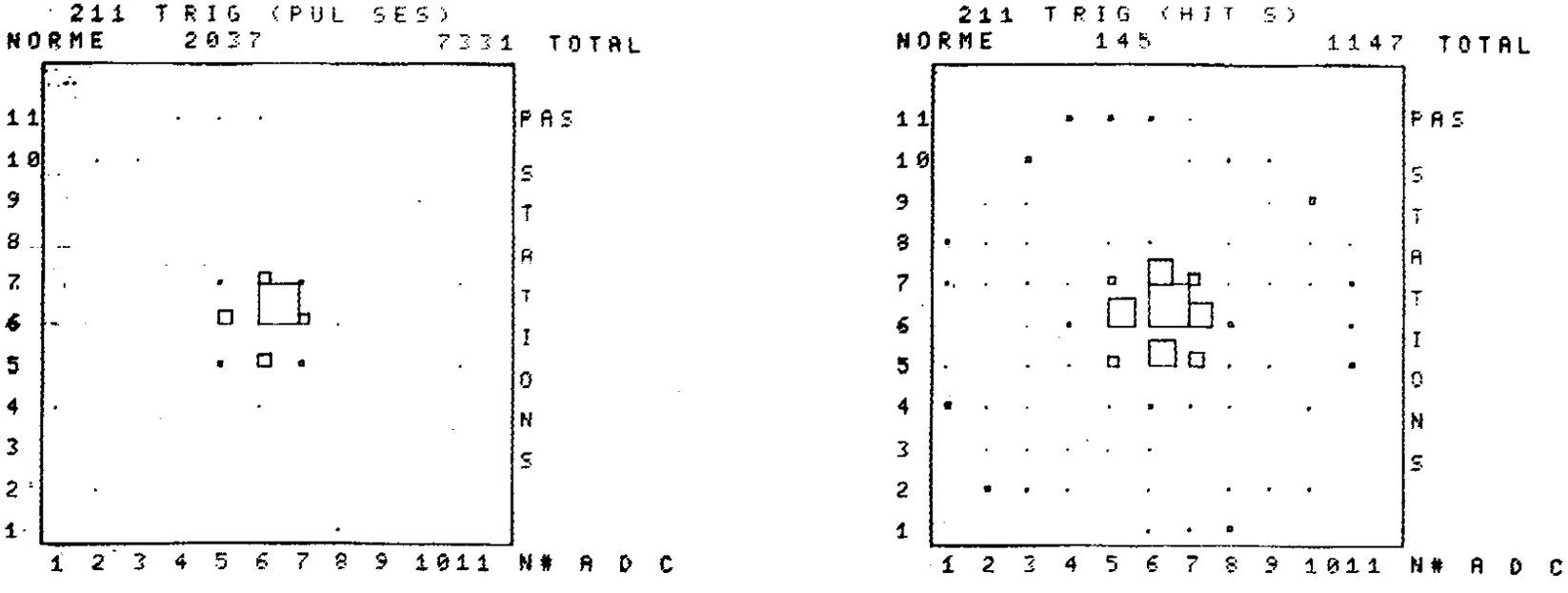
211 TRIG (PULSES)
NORME 2037 7331 TOTAL
PASSTATIONS
1 2 3 4 5 6 7 8 9 10 11
N# A D C
211 TRIG (HITS)
NORME 145 1147 TOTAL
PASSTATIONS
1 2 3 4 5 6 7 8 9 10 11
N# A D C

Fig. 14

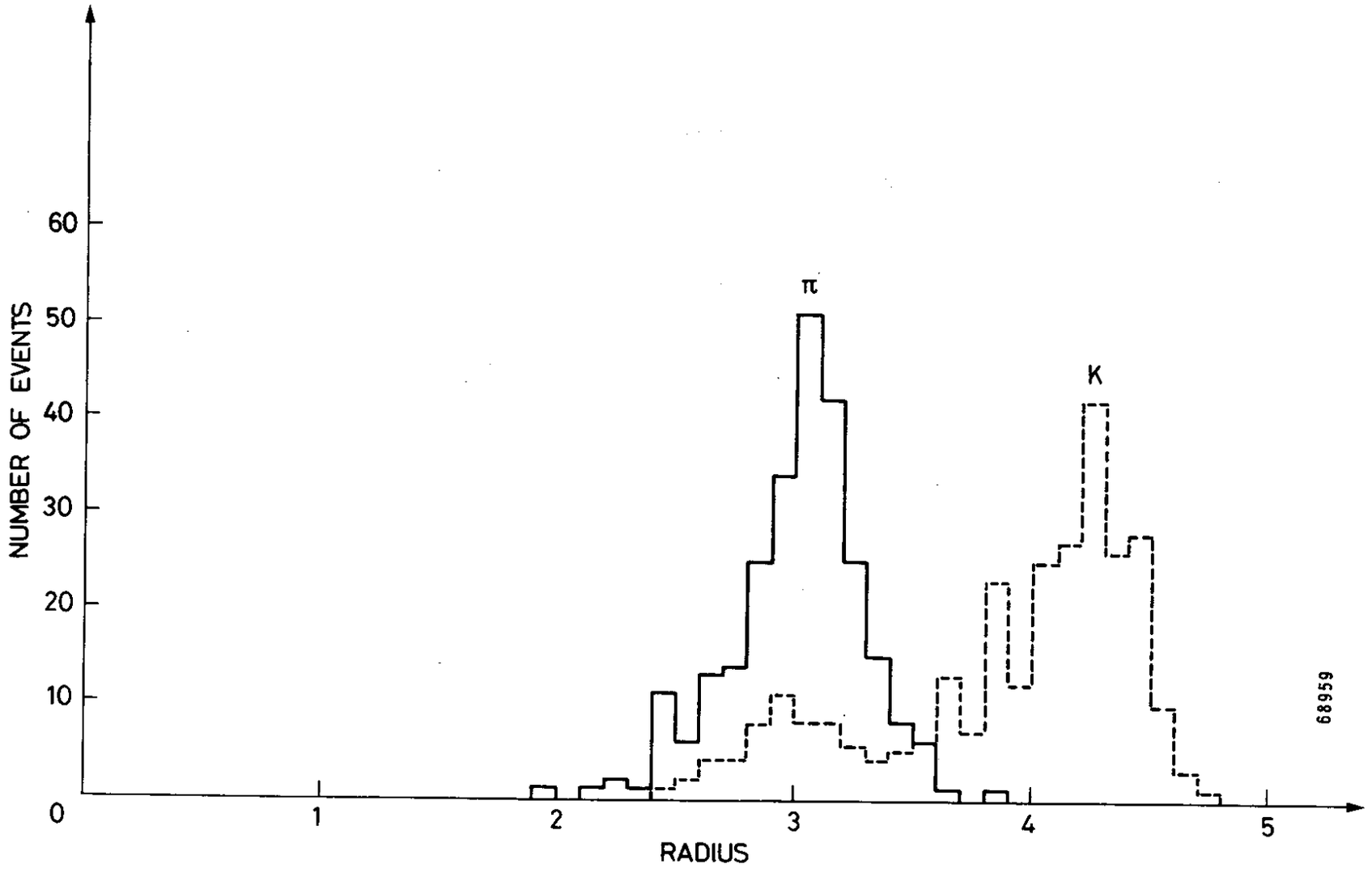


Fig. 15

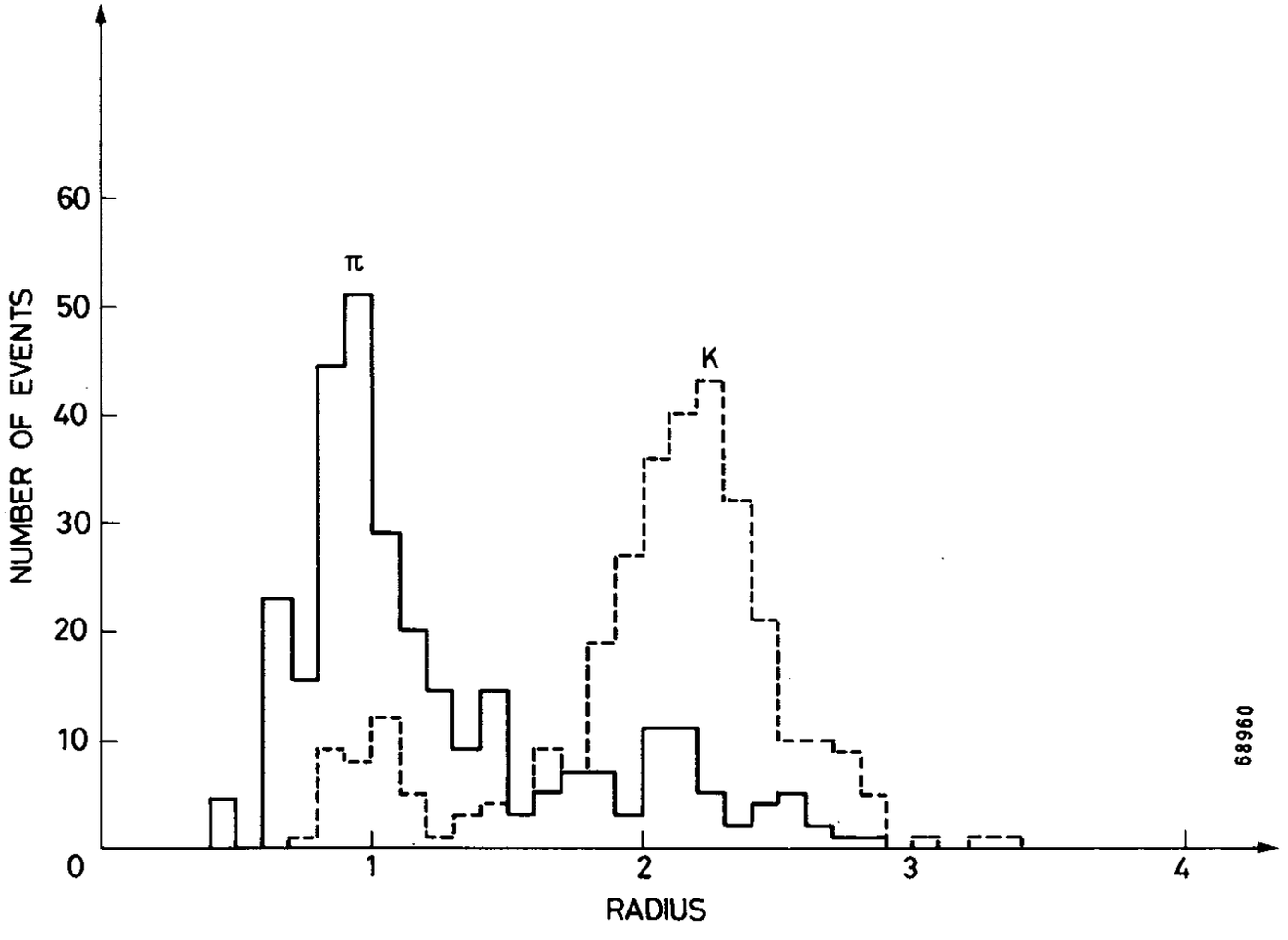


Fig. 16

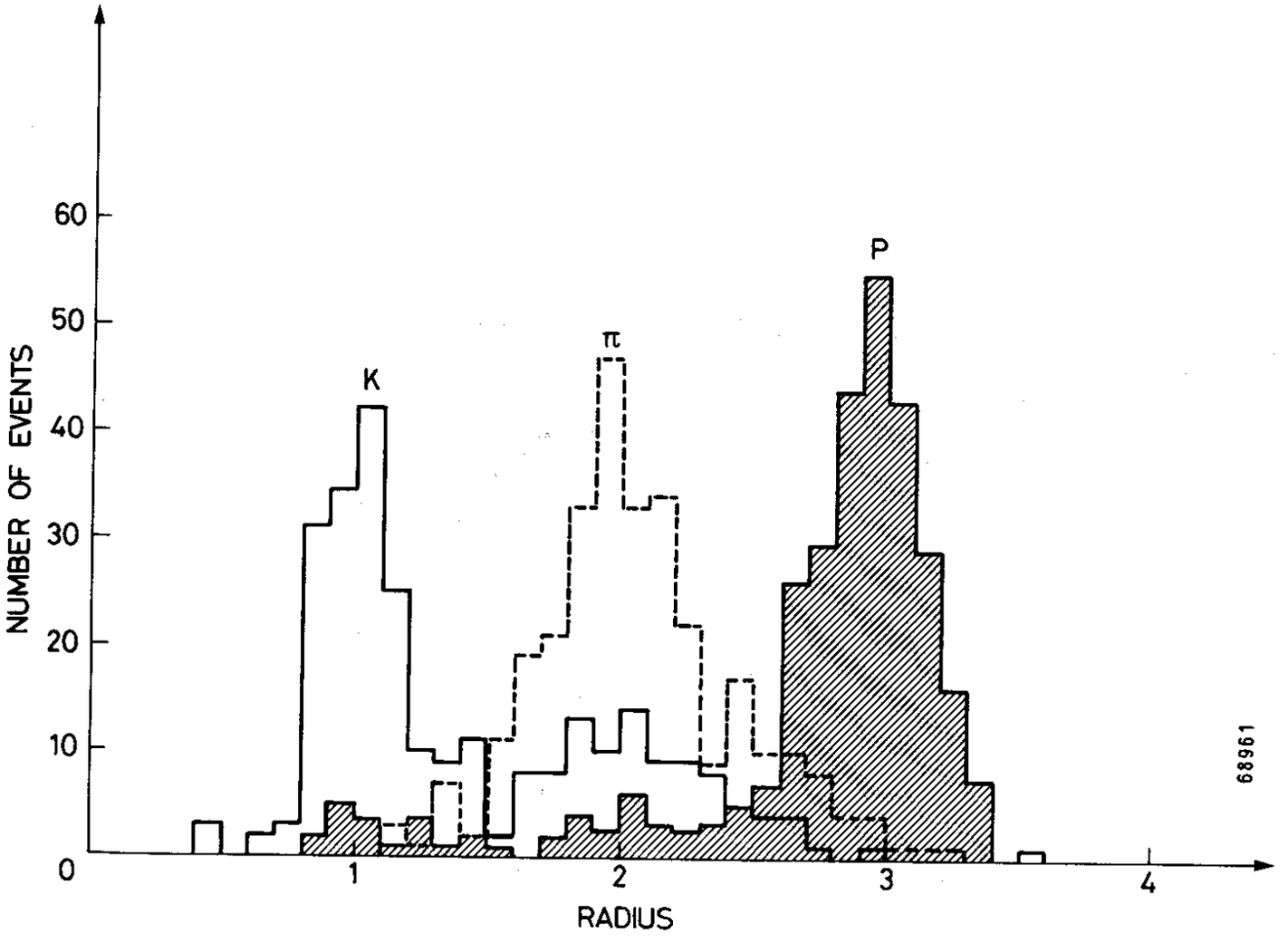


Fig. 17

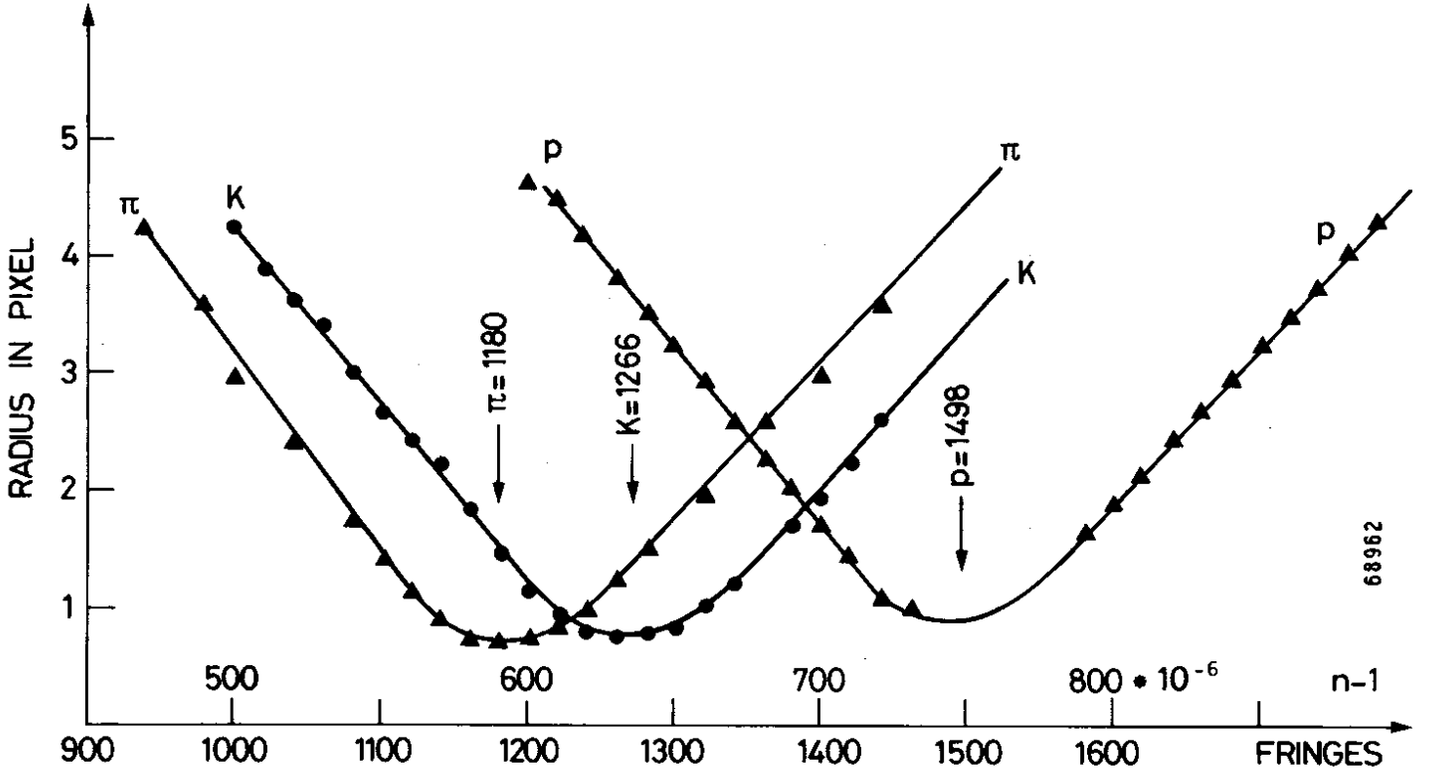
RADIUS IN PIXEL
5
4
3
2
1
π
K
p
π
K
p
π=1180
K=1266
p=1498
68962
500
600
700
800 • 10⁻⁶
n-1
900
1000
1100
1200
1300
1400
1500
1600
FRINGES

Fig. 18

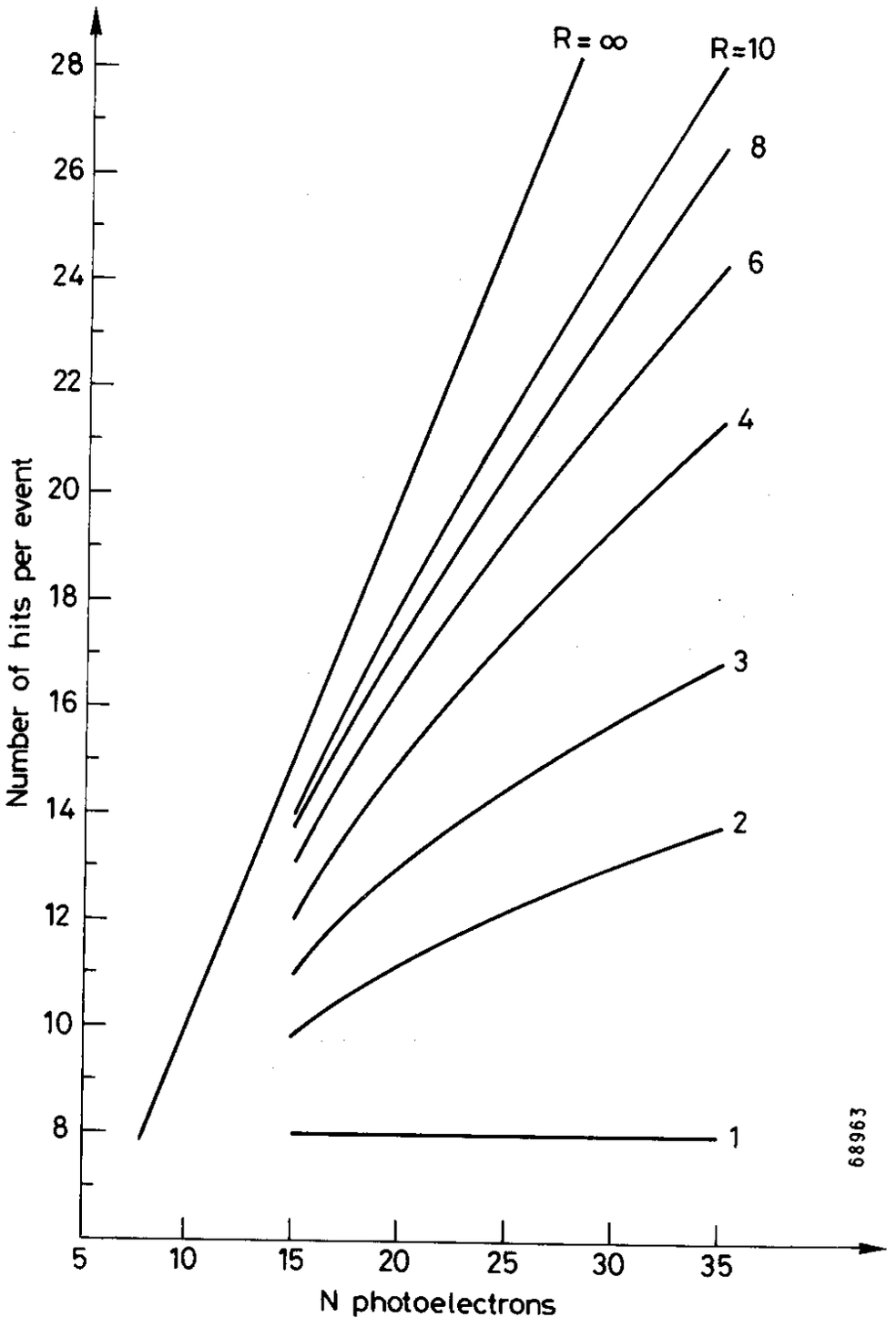
R = ∞
R=10
8
6
4
3
2
1
28
26
24
22
20
18
16
14
12
10
8
Number of hits per event
5
10
15
20
25
30
35
N photoelectrons
68963

Fig. 19

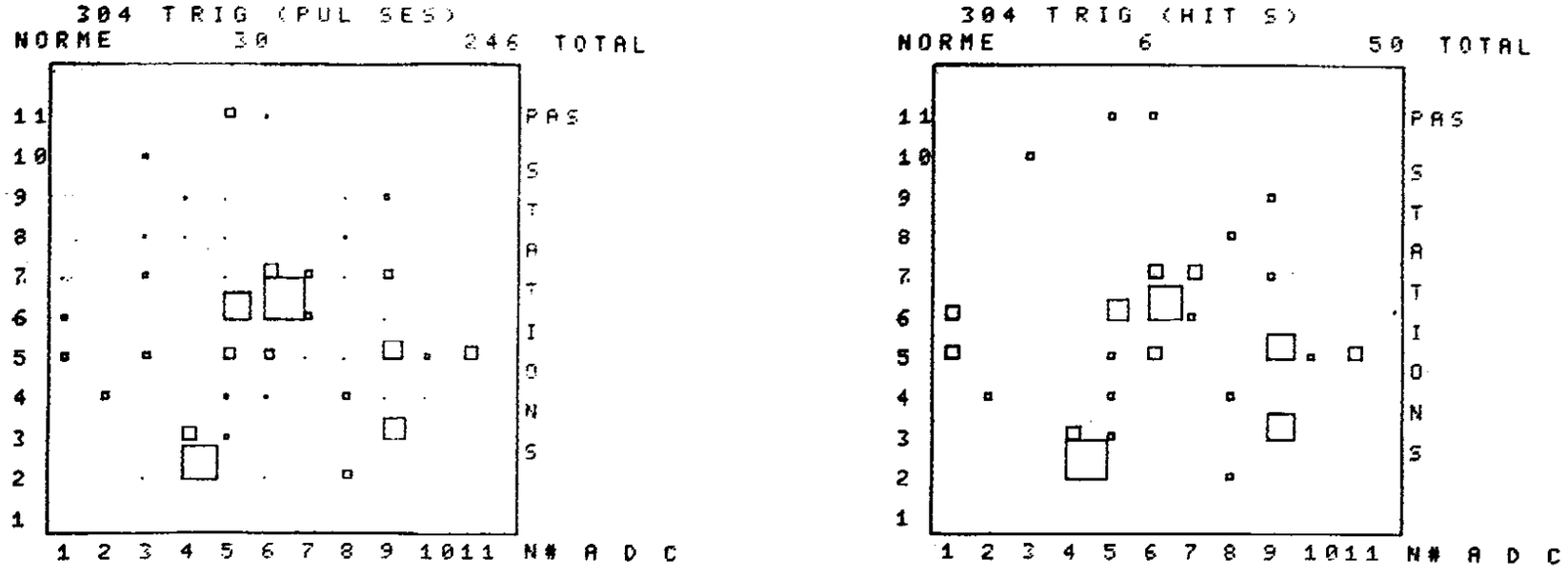
304 TRIG (PULSES)
NORME 30 246 TOTAL
PASSTATIONS
1 2 3 4 5 6 7 8 9 10 11 N# A D C
304 TRIG (HITS)
NORME 6 50 TOTAL
PASSTATIONS
1 2 3 4 5 6 7 8 9 10 11 N# A D C

Fig. 20

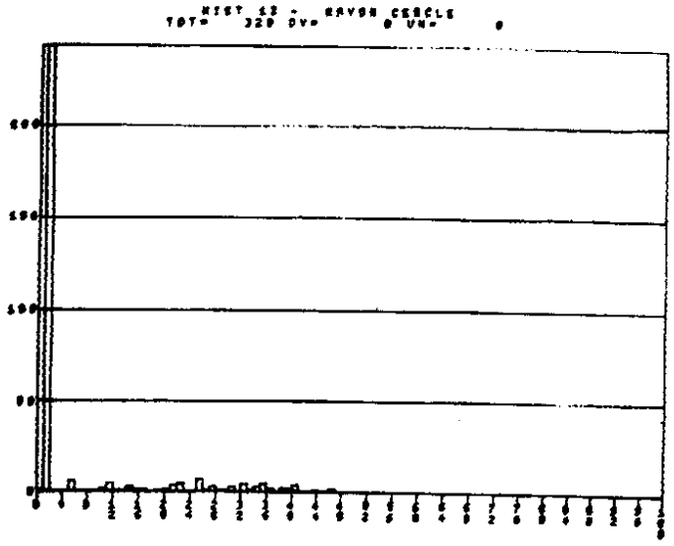

Fig. 21

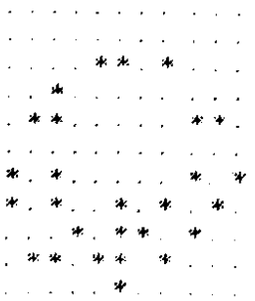

Fig. 22

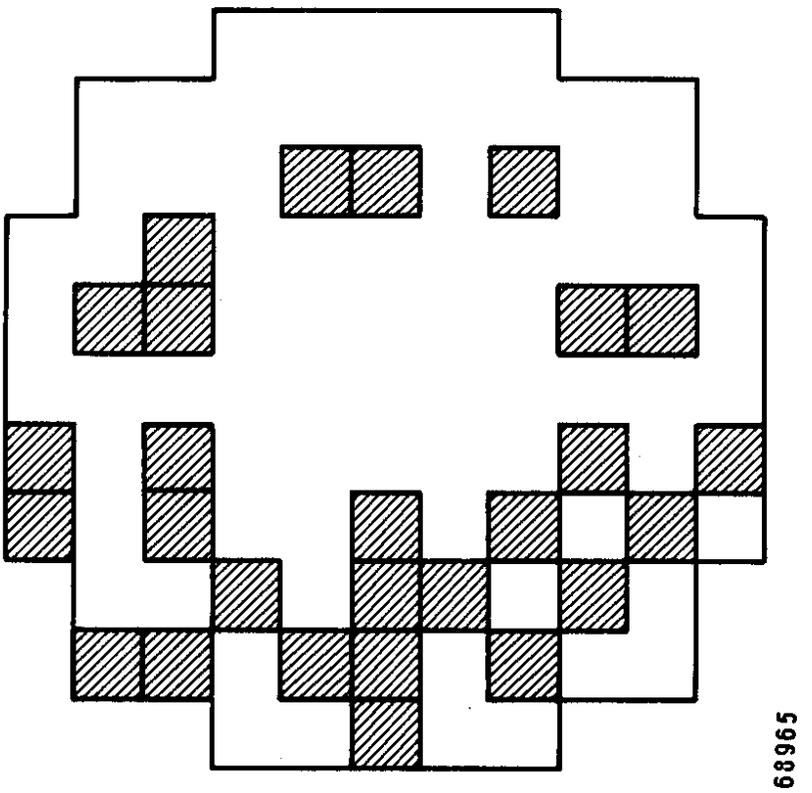


Fig. 23

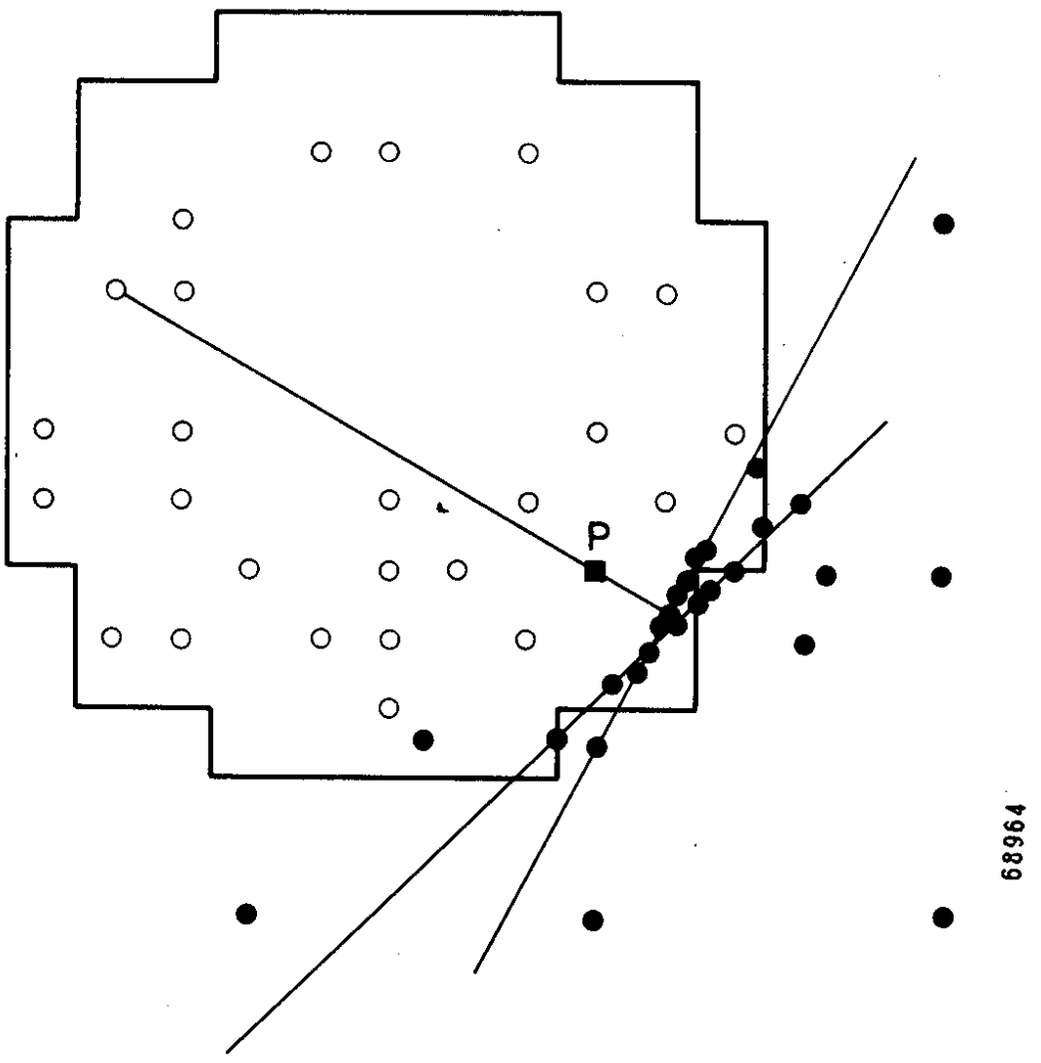


Fig. 24

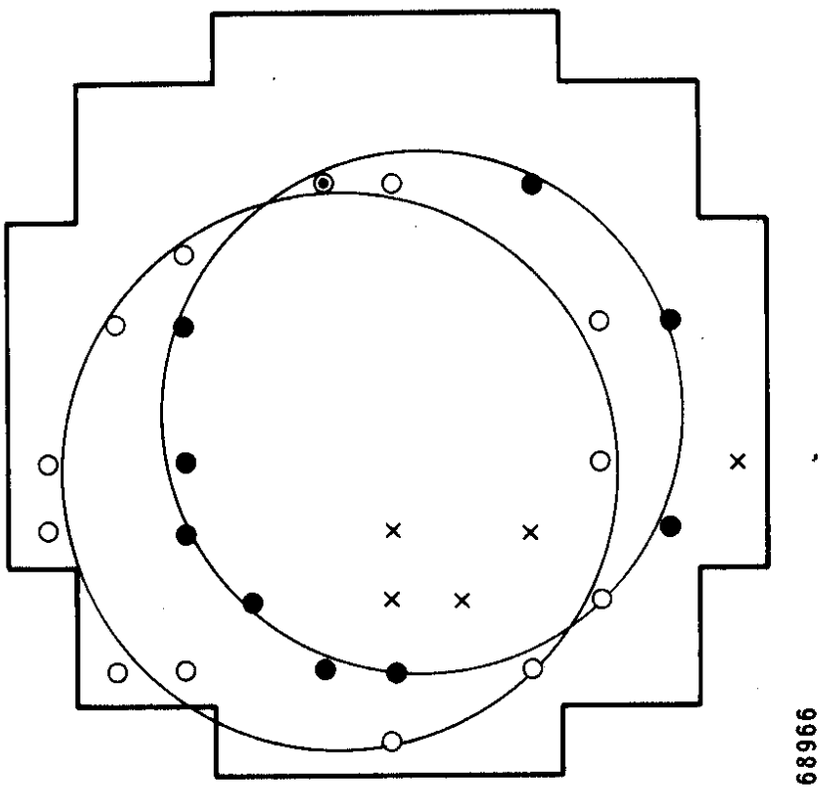


Fig. 25